nature neuroscience

Article

https://doi.org/10.1038/s41593-023-01534-x

Behavior-relevant top-down cross-modal predictions in mouse neocortex

Received: 7 March 2023

Accepted: 27 November 2023

Published online: 4 January 2024

Check for updates

Shuting Han [1] & Fritjof Helmchen [1,2,3]

Animals adapt to a constantly changing world by predicting their environment and the consequences of their actions. The predictive coding hypothesis proposes that the brain generates predictions and continuously compares them with sensory inputs to guide behavior. However, how the brain reconciles conflicting top-down predictions and bottom-up sensory information remains unclear. To address this question, we simultaneously imaged neuronal populations in the mouse somatosensory barrel cortex and posterior parietal cortex during an auditory-cued texture discrimination task. In mice that had learned the task with fixed tone–texture matching, the presentation of mismatched pairing induced conflicts between tone-based texture predictions and actual texture inputs. When decisions were based on the predicted rather than the actual texture, top-down information flow was dominant and texture representations in both areas were modified, whereas dominant bottom-up information flow led to correct representations and behavioral choice. Our findings provide evidence for hierarchical predictive coding in the mouse neocortex.

Predictive processing has long been an attractive theory of the mind. This theory states that the brain is organized hierarchically, with predictions generated in high-level areas passed down to lower areas, and mismatched sensory inputs that do not fit the predictions creating bottom-up flow that represents prediction errors[1]. Despite the computational attractiveness of this model, its implementation in the brain remains elusive. While reward prediction has been studied extensively[2–5], sensory prediction in the neocortex is less understood. It often originates from prior experience, typically through learned associations with other sensory cues, and occurs across many sensory modalities[6–10]. Such prediction can increase the encoding speed and reduce the neural response to expected stimuli in primary sensory areas[6,8], facilitating decisions and behavioral output. Strong sensory predictions can also modify perception, in extreme cases causing hallucination[11–13].

One challenge in studying sensory prediction is to simultaneously observe bottom-up and top-down information. Studies targeting long-range projection axons as a proxy for top-down inputs to local populations have demonstrated that such pathways can indeed modulate sensory perception and decision-making[6,9,14]. However, studies focusing on how neuronal populations along the brain hierarchy represent and transform information, as well as how they communicate with each other, began only recently[15–20]. These studies discovered, for example, that top-down and bottom-up information is channeled through separate activity subspaces[15,16], and that the communication channels are shaped by experience or learning, especially the top-down subspace[18,19,21]. Despite these insights, it is still unknown how top-down predictions and bottom-up sensory inputs interact during behavior and affect behavioral outputs, particularly when they are in conflict.

A key area for routing primary sensory information during active behaviors is the posterior parietal cortex (PPC). PPC is densely interconnected with primary sensory areas such as visual (V1), somatosensory (S1) and auditory (A1) cortex, as well as frontal areas such as the orbitofrontal cortex and the anterior cingulate cortex, and the associative subdivision of thalamus[22]. PPC subserves a wide range of functions including multisensory integration, decision-making, working memory and navigation[22]. In particular, PPC integrates tactile, visual and auditory information in rodents[23–25] and routes relevant sensory

[1]Brain Research Institute, University of Zurich, Zurich, Switzerland. [2]Neuroscience Center Zurich (ZNZ), University of Zurich, Zurich, Switzerland. [3]University Research Priority Program (URPP), Adaptive Brain Circuits in Development and Learning, University of Zurich, Zurich, Switzerland. e-mail: han@hifo.uzh.ch; helmchen@hifo.uzh.ch

information to frontal areas during active behaviors[26–28]. As a key area for multisensory integration, PPC is a candidate for generating cross-modal sensory predictions from previously learned associations. Of particular relevance here is that different subdivisions of PPC engage differentially in processing distinct stimulus modalities—the rostrolateral area (PPC-RL) is activated together with S1 barrel cortex during texture discrimination, whereas the anterior area (PPC-A) activates with auditory cortex areas in auditory discrimination task[26]. These PPC areas are critical for generating sensory associations and transforming sensory information into decisions[26,29–31], making them potential key high-level areas for generating predictions.

Here we aim to better understand how cortical areas along the cortical hierarchy interact when sequential stimuli from two modalities (auditory and tactile) provide task-relevant information. In this case, repeatedly matching specific pairs of auditory-tactile stimuli allows the animal to form predictions about the second stimulus. It is then especially interesting to reveal how regional neural representations and cross-areal interactions are affected when conflicts between predictions and sensory inputs are imposed. Specifically, we focused on the S1 barrel field and PPC subdivisions as representative areas along the hierarchy. We designed a behavioral task with cross-modal sensory predictions (by training mice on matched tone–texture sequence pairs) and then introduced prediction conflicts by occasionally presenting mismatched tone–texture pairs. We used the behavioral choices of mice as a proxy for their perceptual representations. We found that during mismatch, when mice made decisions according to predictions, texture representation in both S1 and PPC was modified. Moreover, these changes only occurred when top-down information flow from the relevant subdivision of PPC was dominant, whereas strong bottom-up information flow from S1 led to both correct texture encoding and corresponding behavioral outcomes. These results demonstrate the impact of predictions on sensory encoding and suggest that the dynamic interaction between top-down and bottom-up information shapes sensory encoding and affects perceptual choice.

Results

An auditory-cued texture discrimination task

To study sensory prediction, we developed an auditory-cued texture discrimination task for mice. Mice were trained to discriminate two textures (rough versus smooth), each associated with a distinct preceding tone (10 kHz versus 18 kHz). Each tone–texture sequence entailed a reward from one of the two lick ports (Fig. 1a,b). During learning, the tone–texture pairing remained fixed, allowing mice to develop specific tone–texture association (matched trials). Then, in expert mice, we randomly presented 10–30% tone–texture mismatches (mismatched trials) to introduce prediction conflicts (Fig. 1b). In these trials, a reward was given according to the tone, to encourage mice to engage in active predictions. For tone–texture mismatches, mice could make the following two types of choices: (1) choose the lick port according to the tone (mismatch–choose–tone or MM→tone trials), indicating that the tone-based prediction, rather than the actual texture stimulus, dominated the decision; (2) choose according to the texture (mismatch–choose–texture or MM→texture trials), indicating that the decision was made based on the actual texture rather than the tone-based prediction (Fig. 1c).

We trained 16 mice expressing GCaMP6f in L2/3 neurons (Methods), all of which could successfully learn the task (Fig. 1d and Extended Data Fig. 1a). Compared to naïve condition, expert mice showed suppressed licking during tone presentation and delayed decision time during texture presentation (Extended Data Fig. 1b–e), indicating that mice associated the tone–texture sequence rather than tone alone with reward. At the end of the experiment, we presented the mice with only tone or only texture, while maintaining the same task structure. With single-modality stimuli, mice still performed above chance level, albeit with a lower success rate, indicating that mice integrated both sensory modalities to make decisions. Furthermore, mice performed better for only texture compared to only tone presentation (Fig. 1e). The latter condition resulted in a higher task disengagement rate (miss rate, Fig. 1f), suggesting that mice regard the missing texture as an incomplete task structure. Finally, testing under texture-only conditions with whiskers removed diminished task performance to chance level (Fig. 1e). Together, these results indicate that mice integrate tone and texture to perform the task, with texture being the most relevant stimulus, presumably due to its closer temporal link to the trial outcome.

In mismatched trials, when an unexpected texture followed the tone, mice decided less likely according to the texture identity than in matched trials (Fig. 1g, correct versus MM→texture; in both these trial types, decisions were according to texture identity). Similarly, the tone biased the choice of mice to a degree not explainable by mere mistakes (Fig. 1g, incorrect versus MM→tone; in both these trial types, decisions were opposite to texture identity). When mice chose according to texture under mismatched conditions, the lick probability during the texture and decision windows was slightly reduced (Fig. 1h (left) and Fig. 1k), indicating lower decision confidence. When mice chose according to tone, mice licked more decisively (Fig. 1h (right) and Fig. 1k), responded faster in general (Fig. 1i) and were more likely to lick before texture onset (Fig. 1j). It is worth noting that in most trials, for all trial types, mice started licking after texture onset (Fig. 1h), indicating that the texture was the most relevant stimulus for the task. These observations were not due to the reward rule in mismatched conditions—the observations were similar when we rewarded mismatched trials according to texture (Extended Data Fig. 1f–i). We also analyzed the movements and pupil diameter of mice. While face and body movements were not substantially different across trial types, the pupil diameter was overall higher in mismatch–choose–texture trials (Extended Data Fig. 1k–m), indicating a higher arousal state that could contribute to mice paying more attention to the texture type. Overall, despite the prominence of the texture stimulus, mice do associate the auditory tone with the following texture stimulus, and the preceding auditory tone does bias the behavior and choice of mice.

Simultaneous imaging of S1 and PPC areas during the task

Using a custom-built two-area two-photon microscope[32], we simultaneously imaged population activity in S1 and PPC when expert mice performed the task (Fig. 2a). Previously, auditory and tactile stimuli were shown to recruit distinct PPC subdivisions—PPC-A and PPC-RL, respectively[26]. To study interactions of cortical areas along the sensory hierarchy, we simultaneously recorded from S1 and PPC-A (9 mice, 40 sessions) or S1 and PPC-RL (14 mice, 91 sessions; 9 mice also had S1 and PPC-A sessions; Fig. 2b). The location of S1 and PPC areas was determined by sensory mapping as well as retinotopic mapping[33] (Extended Data Fig. 2a). We recorded in layer 2/3 across multiple (3–4) depths (100–300 µm), covering 50–600 neurons from each population (Extended Data Fig. 2b,c; Methods). Calcium indicator fluorescence signals from individual neurons and deconvolved spike rates were extracted using Suite2p[34]. All following analysis concerning neuronal activity was performed on deconvolved spike rates.

All three areas were engaged in the task, showing a varying degree of activation across the task windows. We identified task-responsive and discriminative neurons from matched conditions (correct and incorrect trials), using neuronal activity in each task window (Fig. 2c and Extended Data Fig. 2d; Methods). Neurons were defined as task-responsive if their activity level was substantially higher in a specific task window compared to a null distribution generated by randomly sampling frames outside of this window with a matching number of frames. Among the responsive neurons, neurons with substantially higher activity in one task condition versus the other (for

https://doi.org/10.1038/s41593-023-01534-x

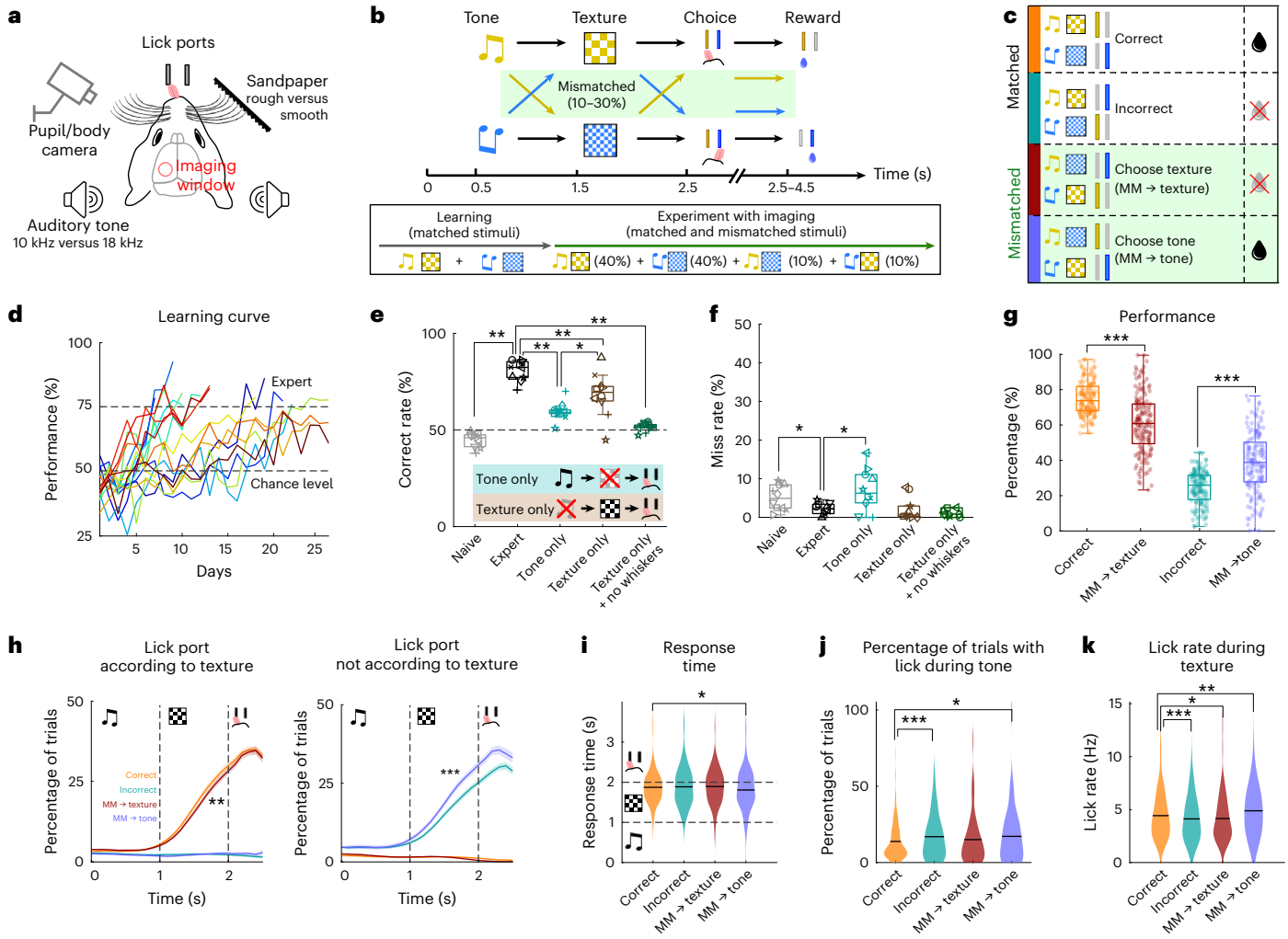

Fig. 1 | Mouse behavior in an auditory-cued texture discrimination task under matched and mismatched conditions. a, Schematic representation of experiment setup with head-fixed mice, with a cranial window over S1 and PPC under a two-photon microscope. **b**, Schematic representation of behavior paradigm. Mice were trained to discriminate two textures paired with distinct auditory tone cues. After mice became experts, tone–texture mismatched trials were introduced. The choice window lasted maximally 2 s, and the reward window was triggered immediately when the mouse licked during this window. **c**, Schematic, nomenclature and color code of different trial types. Trials were categorized based on the contingency of tone, texture and choice. Colored bars on the left indicate the color code of each trial type. **d**, Learning curves of all mice. M30, M33 and M40 were unstable performers (Extended Data Fig. 1a). **e**, Performance in single-modality experiments, in which only tone, only texture or only texture without whiskers was presented. Markers indicate individual mice. The outlier (star) is M40 in **d**. **f**, Miss rates for experiments in **e**. **g**, Percentage of each trial type for matched and mismatched conditions. **h**, Lick probability over trial time on the lick ports according to texture identity (left) or the opposite lick port (right), calculated as a percentage of trials in each session with a lick event at each given time point. **i**, Response time for different trial types. **j**, Percentage of trials in each session, in which licks on the final choice spout were recorded during tone presentation. **k**, Lick rate during texture presentation for different trial types. (**e** and **f**: $n = 10$ mice, one session per mouse; naïve was the average of first three sessions, and expert was the average of best three sessions; **g**–**k**: $n = 16$ mice, total 148 sessions; Wilcoxon signed-rank test; $^{*}P < 0.05$, $^{**}P < 0.01$, $^{***}P < 0.001$; for exact P values, see Supplementary Table 1).

example, texture 1 versus texture 2) were defined as discriminative neurons. Although S1 and both PPC-A and PPC-RL displayed the highest task-related activity during the texture window, PPC-A had the highest fractions of both task-responsive and discriminative neurons in the remaining tone, choice and reward windows (Fig. 2d,e), indicating its higher position in the hierarchy. In addition, both tone and texture neurons were more abundant in the medial part of PPC-A (Extended Data Fig. 2e). PPC-RL was less involved than PPC-A during sensory processing, but was also more engaged than S1 after reward delivery. In PPC-A, joint-responsive neurons for tone and texture accounted only for a small percentage. Texture and choice, however, shared about 20% of overlapping neurons (Fig. 2f). Overall, S1 was most tuned to texture processing, PPC-A was engaged throughout the trial time, and PPC-RL was involved in texture and reward processing.

Tone–texture mismatch alters texture neuron tuning

We first asked whether tone-based prediction could alter texture-evoked responses of single neurons. To answer this question, we analyzed the response amplitude of tone- and texture-discriminative neurons. While tone-discriminative neurons showed differential responses to the distinct tones, they did not show significant trial type-dependent selectivity (Extended Data Fig. 3). In contrast, the activity of texture-discriminative neurons could be altered by the tone. In S1, texture-discriminative neurons showed texture selectivity only in mismatch–choose–texture trials. When mice chose according to tone, these neurons showed mixed preferences, responding to a combination of expected and actual textures (Fig. 3a–c, top rows). Similar results were obtained in PPC-RL (Fig. 3a–c, bottom rows). In PPC-A, the texture-discriminative neurons showed a strong preference to the

https://doi.org/10.1038/s41593-023-01534-x

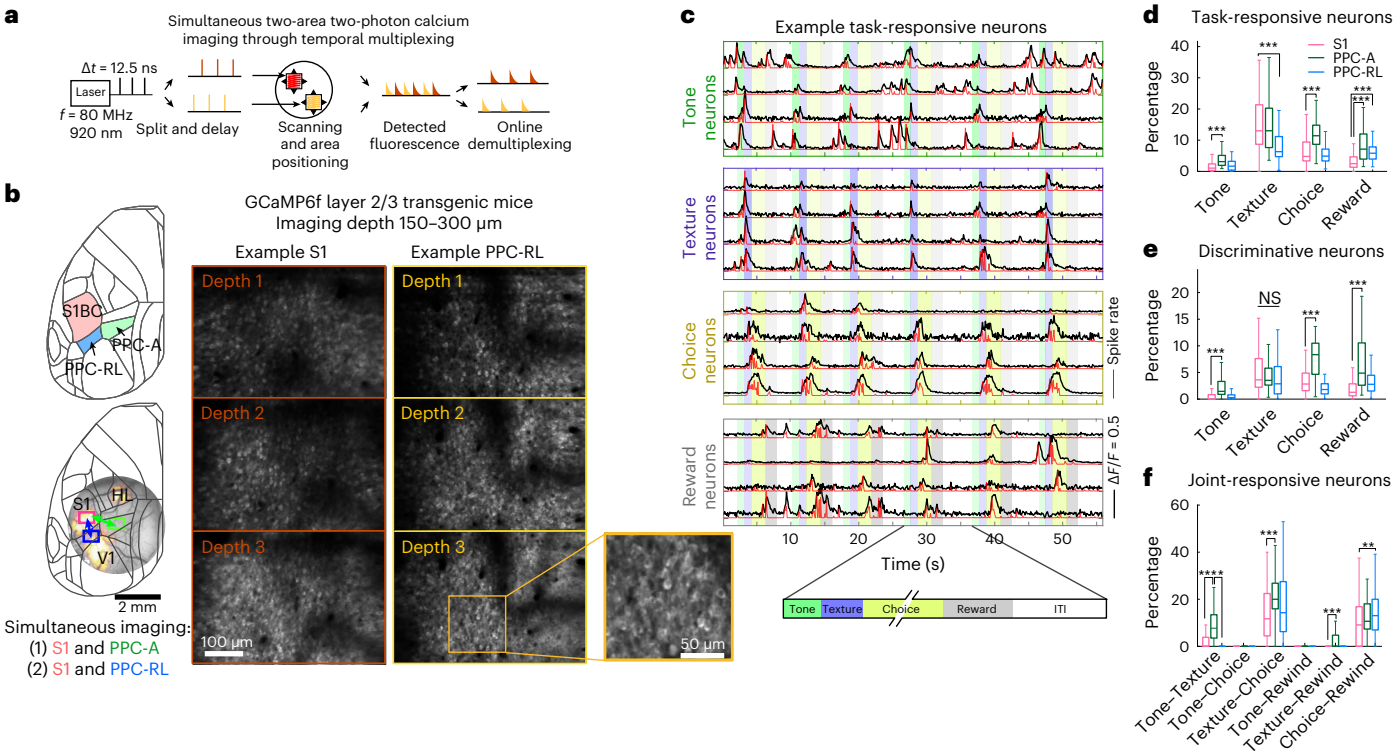

Fig. 2 | Simultaneous two-photon imaging of task-related S1 and PPC activity. **a**, Temporal multiplexing-based simultaneous two-area two-photon imaging. Laser pulses were split into two copies, one of which was delayed by half of the pulse interval. Each copy was directed to an independently positioned FOV, and the emitted fluorescence was demultiplexed online with fast acquisition hardware. **b**, Left, locations of S1, PPC-RL and PPC-A on the left hemisphere (top). Example widefield sensory mapping response, as well as example FOV locations, are shown in the bottom panel. Right, example FOVs of simultaneously imaged S1 and PPC-RL. **c**, Example $\Delta F/F$ traces (black) and spike rates (red) of task-responsive neurons. ITI, intertrial interval. **d**, Percentage of task-responsive neurons for each task window in S1, PPC-RL and PPC-A. **e**, Percentage of discriminative neurons for each task variable in the three areas. **f**, Percentage of joint-responsive neurons (neurons that are responsive in two task windows). The percentage was calculated as $n_i \cap n_j / n_i \cup n_j$, where n_i and n_j are sets of responsive neurons for task phases i and j. (S1: 14 mice and 118 sessions, PPC-RL: 14 mice and 78 sessions, and PPC-A: 9 mice and 40 sessions; Wilcoxon rank-sum test; *P<0.05; **P<0.01; ***P<0.001; NS, nonsignificant; Supplementary Table 1).

expected rather than the actual texture when mice chose according to tone, but not when they chose according to texture (Fig. 3a–c, middle rows). This could not be explained by the choice selectivity of texture neurons or licking behavior, because we observed the same effect in PPC-A texture neurons that were not choice-selective as well as in trials with no early licks (Extended Data Fig. 4). To further exclude the influence of choice-related activity, we applied a generalized linear model (GLM) model to identify texture and choice neurons from the mean activity in the texture window, which yielded a similar number of texture and choice neurons and revealed similar texture selectivity change in mismatch–choose–tone trials (Extended Data Fig. 5). It is worth noting that in all our analysis, this inverted texture preference is distinct from the response distribution observed for incorrect trials, where the texture–choice pairing is the same (choice not according to the texture). These results provide strong evidence that tone-based prediction can shift the texture representation of individual neurons in PPC-A to the expected texture while disrupting the texture representation in PPC-RL and S1.

Tone–texture mismatch alters population encoding

To further investigate the encoding of different task variables in neuronal populations of these three areas and representational changes, we trained linear support vector machine (SVM) decoders on the population activity patterns to discriminate tone, texture, choice and reward (Fig. 4a–e and Extended Data Fig. 6a–c). Each decoder was trained and cross-validated using the time-concatenated spike rates of all neurons from the corresponding task window (for example, texture window for the texture decoder; Fig. 4a) and from matched trials (correct and incorrect trials). Each classifier defines a hyperplane that best separates the two variables. By projecting the population firing rate onto the orthogonal axis of this hyperplane, or the 'projection axis,' we could estimate the encoding strength of the task variables over trial time[10] (Fig. 4a; Methods).

Among the three areas, PPC-A encoded tone information best (Fig. 4b (top) and 4c), consistent with PPC-A showing the highest fraction of tone-tuned neurons. While tone encoding was stronger in the tone window, it persisted after texture onset (Fig. 4d). Interestingly, tone encoding strength coincided with behavioral choice—in mismatch–choose–texture trials, PPC-A tone encoding was weaker compared to correct trials (Fig. 4c), but not in mismatch–choose–tone trials. In the latter case, the tone (and thus the expected texture) was still decodable during texture presentation (Fig. 4d, middle). We observed similar results in S1 and PPC-RL despite their weaker tone encoding. These observations are consistent with our findings that the tone could bias the behavior and choice of mice.

All three areas strongly encoded texture (Fig. 4b, bottom). Consistent with the results in single neurons, in mismatched trials, the actual texture was encoded by the populations only when mice chose texture, although weaker compared to correct trials. When mice chose tone, the expected texture was encoded instead (Fig. 4e). The timing of texture encoding is also worth noting. In matched correct trials, the actual texture was encoded slightly before texture onset, indicating an

https://doi.org/10.1038/s41593-023-01534-x

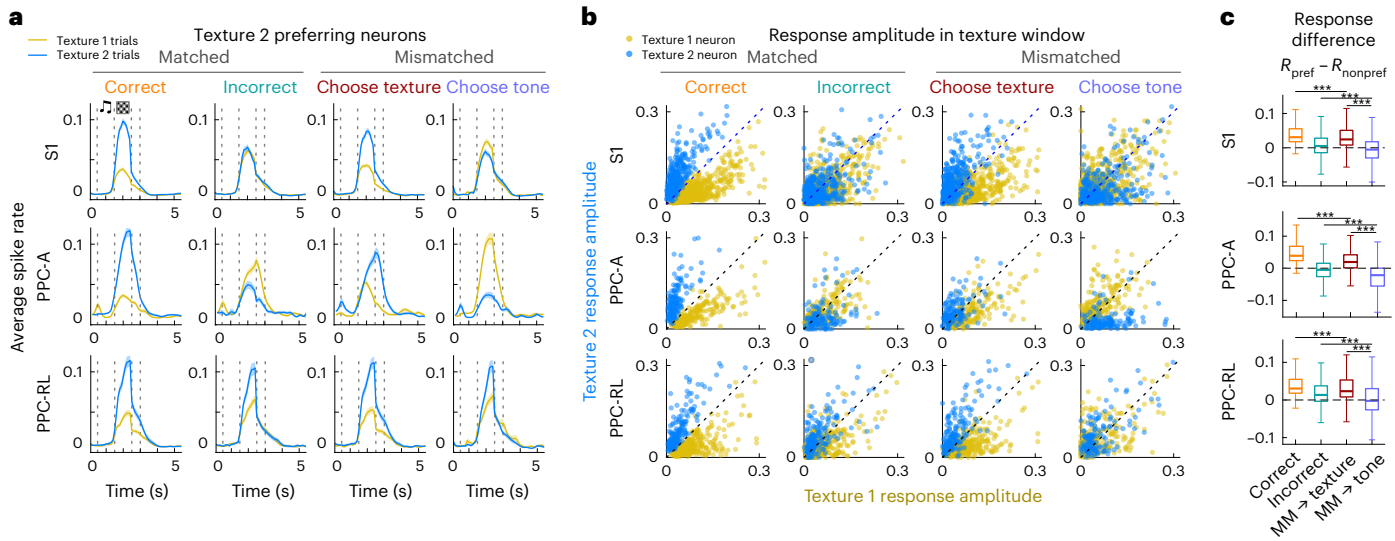

Fig. 3 | Tone–texture mismatch alters neuronal tuning to texture. a, Average normalized spike rate of texture 2 discriminative neurons in S1, PPC-RL and PPC-A, in matched and mismatched trials. The spike rate of each neuron was normalized to be between 0 and 1 within each session. **b**, The mean response amplitudes of all texture-discriminative neurons in the texture window. Plots are shown across areas (rows) and trial types (columns). Each dot represents the responses of one neuron in one imaging session. **c**, Selectivity index of the texture-discriminative neurons during texture window, in different trial types. The selectivity index was calculated as the difference between the average response to the preferred texture (R_{pref}) and the average response to the nonpreferred texture ($R_{nonpref}$) (S1: 1,486 neurons, PPC-A: 400 neurons and PPC-RL: 618 neurons; Wilcoxon rank-sum test; $^{***}P < 0.001$; Supplementary Table 1).

active ongoing prediction (Fig. 4b, bottom left). However, in mismatch–choose–texture trials, although the texture was encoded correctly, this early texture encoding was absent (Fig. 4b, bottom middle right). In addition, PPC-A texture encoding lagged behind S1 and PPC-RL, suggesting that the integration of texture and tone stimuli was impaired by the mismatched tone, an effect particularly strong in PPC-A. On the other hand, in mismatch–choose–tone trials, the expected texture was encoded slightly before texture onset, and texture encoding in PPC-A preceded that of S1 and PPC-RL (Fig. 4b (bottom right) and Extended Data Fig. 6c). These results indicate that the tone facilitated the encoding of the expected texture. This early texture encoding was not due to choice-related activity, as choice could not be decoded during the tone window in these trials (Extended Data Fig. 6b). In addition, texture decoder axes of incorrect trials did not resemble that of mismatch–choose–tone trials (Extended Data Fig. 6f). These results suggest that tone information in PPC-A led to the encoding of the expected texture across S1 and PPC.

We next wondered whether the tone alone was sufficient to evoke predictive texture encoding. We trained linear classifiers for tone-only and texture-only sessions and indeed found that tone alone led to correct texture encoding in PPC-A (Fig. 4f,g, left). In contrast, the lack of a preceding tone reduced texture encoding speed and strength in PPC-A (Fig. 4f,g, right), but choice engaged both S1 and PPC (Extended Data Fig. 6d,e). Thus, PPC-A is able to generate predictive texture information from the preceding tone, likely through multisensory integration mechanisms, and it serves as a center for routing and transforming sensory information into decisions.

Interareal interaction between S1 and PPC during task

We next asked if such predictive information could be explained by top-down and bottom-up interactions between S1 and PPC areas. We started by characterizing the interaction structure of S1 and PPC populations during the task. To measure the population interactions, we used canonical correlation analysis (CCA) due to its symmetric way of treating the two populations. CCA has been applied to analyze the interareal interactions in several recent studies[16,17,19]. Conceptually, the activity of a neuronal population can be represented in a high-dimensional space, where each dimension represents the activity of one neuron in this population. For the simultaneous activity of two populations, CCA finds pairs of dimensions that maximize the correlation between the projections of the two populations (Fig. 5a; Methods). These pairs of dimensions (canonical dimensions) define the shared interaction axes of the two populations at this time point.

Stable CCA models depend on having a sufficient amount of data (time points) compared to the number of variables (neurons)[35]. To increase computation stability, we first applied principal component analysis (PCA) to both populations and kept the first 30 components. Because we are interested in the population interaction structure, we also subtracted the stimulus-triggered average, keeping only the residual activity that captures trial-to-trial covariation. To capture the dynamic interaction over trial time, we applied CCA to a 0.5-s sliding window (Fig. 5b). Overall, the interaction between S1 and PPC-A was stronger than S1 and PPC-RL (Fig. 5c,d). We further characterized the communication subspace between S1 and PPC by computing the number of significant canonical dimensions, where the canonical correlation is above the chance level. Consistent with previous reports[15,16], S1 and PPC overall interacted in a low-dimensional space, with S1 and PPC-A interacting in more dimensions than S1 and PPC-RL during tone and texture windows (Fig. 5e–g), indicating PPC-A was more involved in sensory processing during the task.

Top-down and bottom-up interactions govern behavioral choice

In behavioral tasks, sensory information flows through the cortical hierarchy to generate decisions. For our task, we asked whether the behavioral choice of mice under mismatch conditions could be explained by the net effect of top-down (prediction) and bottom-up (sensory) information flow. Conceptually, mismatch–choose–texture trials could be explained by stronger bottom-up information from S1 than top-down information from PPC, whereas mismatch–choose–tone trials could be explained by the opposite. To test this hypothesis, we measured the strength of bottom-up and top-down information flow by introducing a temporal lag in CCA. We defined bottom-up strength

https://doi.org/10.1038/s41593-023-01534-x

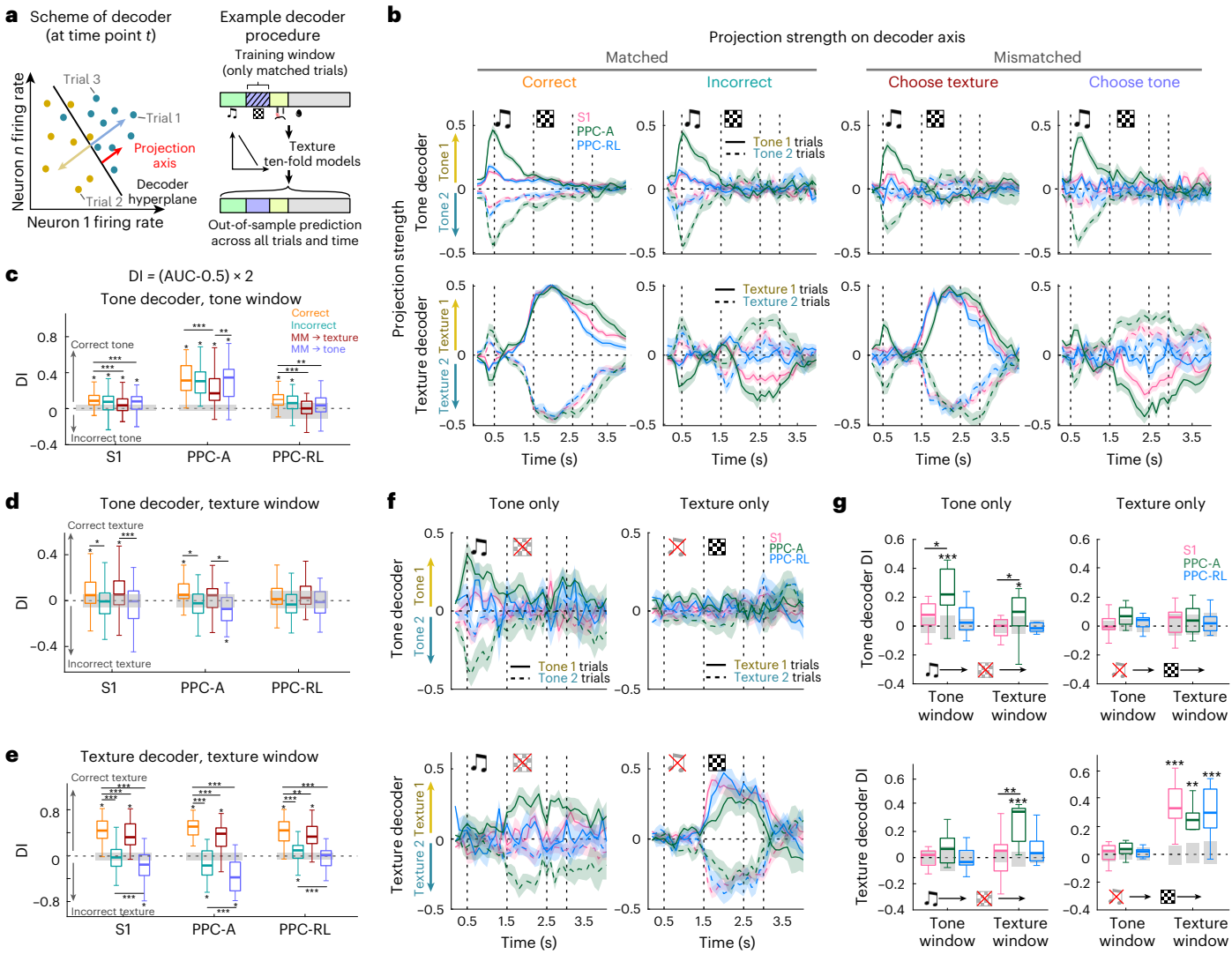

Fig. 4 | Tone–texture mismatch alters texture encoding in S1 and PPC populations. a, Left, scheme of the decoders. Black line represents the decoder hyperplane; yellow and teal dots represent the neuronal population activity at a given time point in the trial; each dot was projected onto the orthogonal axis of the decoder hyperplane to represent the decoder confidence. Right, example procedure for texture decoding. **b**, Neuronal population decoding of tone (top) and texture (bottom). Sensory encoding is represented by projection strength on the axes of linear decoders trained to discriminate tone and texture, in the tone and texture window, respectively. Line colors indicate area identity (magenta, S1; green, PPC-A; and blue, PPC-RL); solid and dash lines indicate stimulus identity in the trial. **c**, DI of tone decoder in the tone window. Asterisks above each box indicate significance compared to shuffled data (gray bars), for which neuron identities were shuffled, while trial and time correspondences were kept the same. Asterisks across boxes indicate a comparison between trial types. **d**, DI of tone decoder in texture window. **e**, DI of texture decoder in texture window. **f**, Decoder projection strength of tone (top row) and texture (bottom row) in single-modality experiments. **g**, DI of tone decoder and texture decoder in single-modality experiments, in tone window and texture window, separately. Asterisks are represented as in **c** (S1: 14 mice and 118 sessions, PPC-RL: 14 mice and 78 sessions, and PPC-A: 9 mice and 40 sessions; Wilcoxon rank-sum test was used for comparison with shuffled data and Wilcoxon signed-rank test for comparison between trial types; $^{*}P < 0.05$; $^{**}P < 0.01$; $^{***}P < 0.001$; Supplementary Table 1).

by moving the S1 activity window ahead of PPC and averaging the top canonical correlation across lags (over 0.3 s), and top-down strength by moving PPC activity ahead of S1, respectively (Fig. 6a). We represented net information flow by an index that was defined as the difference between bottom-up and top-down strengths normalized by the total interaction strength (Fig. 6a).

In matched trials, S1 and PPC-A interaction showed strong bottom-up dominance during texture presentation (Fig. 6b,d,e, correct). In mismatch–choose–texture trials, both tone and texture windows were dominated by bottom-up information (Fig. 6b,d,e, MM→texture), coinciding with slightly elevated bottom-up flow during the prestimulus window (Fig. 6d,e; 0.029 ± 0.014 versus 0.006 ± 0.016) and a higher arousal state in these trials (Extended Data Fig. 1j,m). In contrast, in mismatch–choose–tone trials, tone presentation was accompanied by top-down information flow, which persisted throughout texture presentation (Fig. 6b,d,e, MM→tone). This top-down dominance was also observed from PPC-RL to S1 during tone presentation (Fig. 6c,f,g), indicating an internal state that emphasized top-down inputs.

The information flow between S1 and PPC showed similar patterns in single-modality experiments (Extended Data Fig. 7). In tone-only sessions, the population interaction resembled that of mismatch–choose–tone trials, that is, top-down flow from PPC-A to S1 in the tone window persisted throughout the texture window (without texture), consistent with a role of PPC-A in tone-based predictions. In texture-only sessions, bottom-up flow from S1 to PPC-A during texture

https://doi.org/10.1038/s41593-023-01534-x

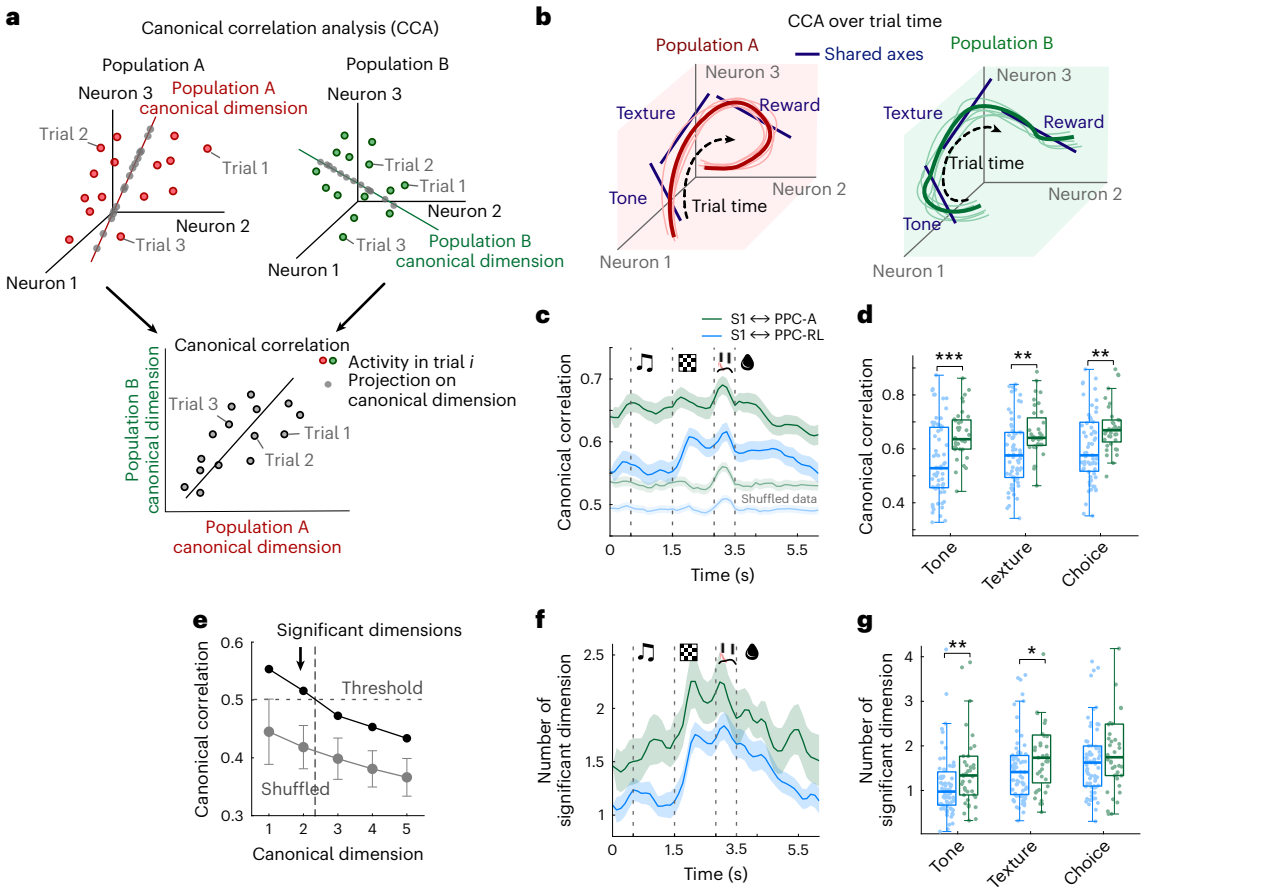

Fig. 5 | Interaction pattern of S1 and PPC areas during the behavioral task. **a**, Illustration of CCA. The activity of each neuronal population can be represented as points in a high-dimensional space, where each dimension represents the activity of one neuron in this population. At a given time point in the trial, CCA identifies a set of canonical dimensions through linear combinations of variables from the two populations that have maximum correlation. **b**, Illustration of defining separate CCA axes over the trial time. **c**, Top canonical correlation between S1 and PPC-A (green) and S1 and PPC-RL (blue). Light colors indicate shuffled correlation, where only the trial correspondence between the two areas was shuffled, while the trial structure was kept the same. **d**, Average canonical correlation strength of **c** in each task window. **e**, Number of significant interaction dimensions was determined by generating shuffled correlations and defining a threshold (mean + 3 s.d.) using the first correlation values. Canonical dimensions in real data with correlations higher than this threshold were considered significant. Example is from one imaging session. **f**, Number of significant dimensions in S1 and PPC-A and S1 and PPC-RL pairs. **g**, Average number of significant dimensions of **f** in each task window (S1↔PPC-A: 9 mice and 40 sessions and S1↔PPC-RL: 13 mice and 71 sessions; Wilcoxon rank-sum test; $^{*}P < 0.05$; $^{**}P < 0.01$; $^{***}P < 0.001$; Supplementary Table 1).

presentation occurred instead, resembling the interaction observed for mismatch–choose–texture trials. To exclude the possibility that these observations were specific to the CCA method, we alternatively computed population interaction strength with Pearson correlation. Overall, all results were reproduced, although the Pearson correlation does not capture the optimal interaction between populations (Extended Data Fig. 8).

To investigate whether such interareal interactions could be reflected by the response strength of S1 and PPC on a single-trial basis, we compared the normalized decoder projection strength of S1 and PPC-A in individual trials. Although texture encoding strengths of S1 and PPC-A were similar in correct and mismatch–choose–texture trials, PPC-A showed stronger texture encoding than S1 in mismatch–choose–tone trials (Extended Data Fig. 9a,b). In the latter trials, the encoding coefficient of PPC-A tone response versus S1 texture response was also elevated, indicating that the tone in PPC-A was weighted more than the texture information in S1 compared to other trial types (Extended Data Fig. 9c,d). Additionally, the texture/tone encoding coefficient within PPC-A was higher in mismatch–choose–texture and lower in mismatch–choose–tone trials, indicating that, in PPC-A, texture was weighted more in mismatch–choose–texture trials, whereas tone was weighted more in mismatch–choose–tone trials (Extended Data Fig. 9e,f). These findings further support our observation of different top-down and bottom-up interactions underlying these conditions.

Our task design allowed the mice to rely either more on tone-based prediction or more on the texture input in their behavior. We wondered whether these different states were accompanied by different neuronal representations even in correct trials, where tone and texture were paired normally. We approximated the state of mice from their choices under mismatch conditions. We defined texture-preferring sessions as the top ten sessions where mice were more prone to choose texture in mismatch conditions, and tone-preferring sessions as the top ten sessions where mice were more prone to choose tone (Extended Data Fig. 10a). We observed both behavioral and neural differences between these two sets of sessions. Behaviorally, mice showed slightly shorter response time, higher probability of licking during tone and higher lick rate during texture presentation in tone-preferring versus texture-preferring sessions (Extended Data Fig. 10b–e). On the neuronal level, in tone-preferring sessions, with comparable numbers of tone neurons in S1 and PPC-A, tone decoding was stronger and top-down information flow from PPC-A to S1 was enhanced, suggesting a more efficient transfer of tone information. On the other hand, in

https://doi.org/10.1038/s41593-023-01534-x

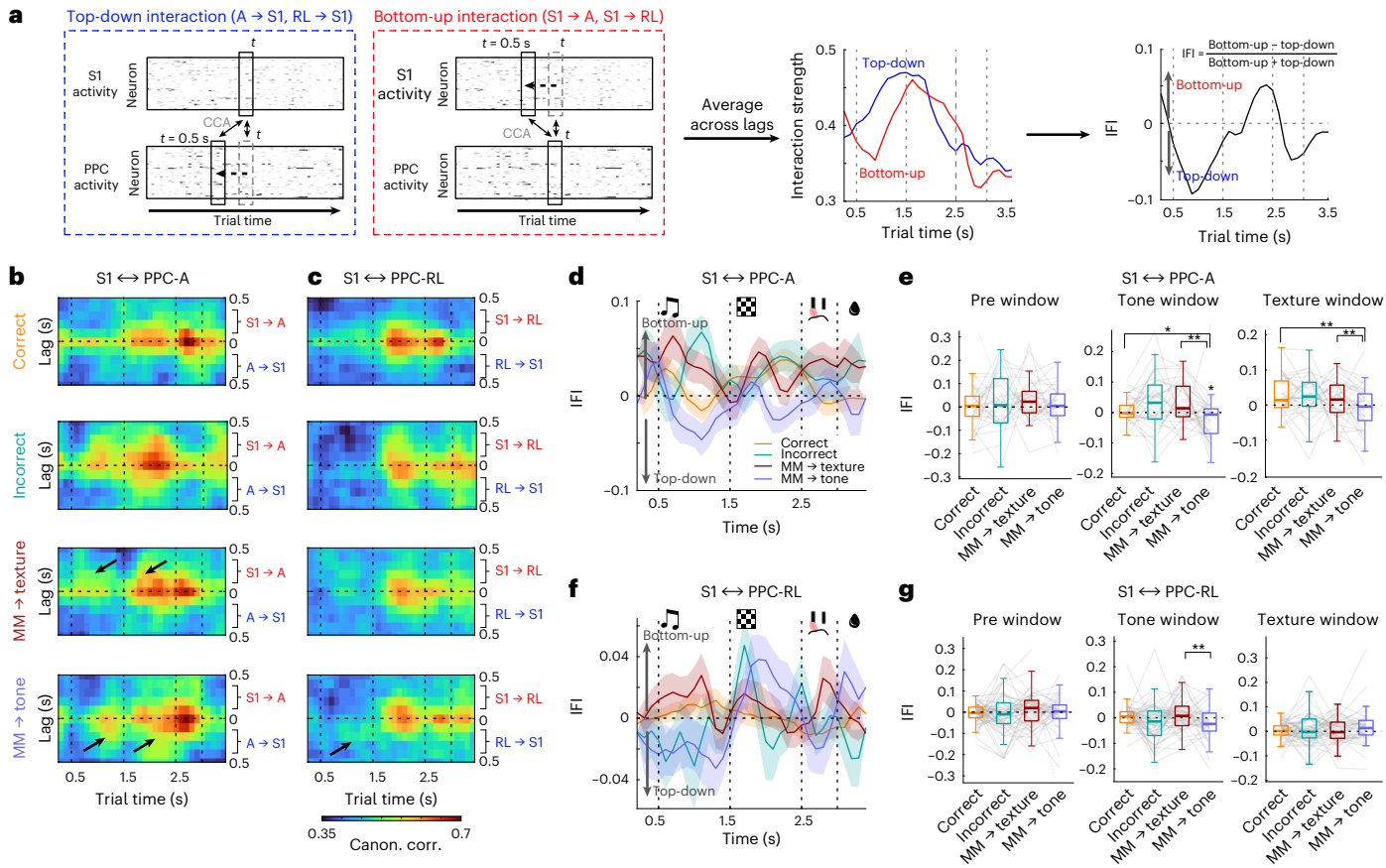

Fig. 6 | Top-down and bottom-up interactions between S1 and PPC areas during prediction mismatches. a, Top-down interaction strength (PPC-A/RL to S1) was calculated by the average canonical correlation with a negative lag for PPC, and bottom-up interaction strength was calculated by the average correlation with a negative lag for S1 (left and middle). The direction and strength of the S1–PPC interaction were characterized by the IFI, defined as the ratio of the difference between the two interactions to their sum (right). **b**, Lagged canonical correlation between S1 and PPC-A, averaged across all sessions, for different trial types. **c**, IFI computed from **b**. **d**, Quantification of IFI between S1 and PPC-A. **e**, Lagged canonical correlation between S1 and PPC-RL, averaged across all sessions, for different trial types. **f**, IFI computed from **e**. **g**, Quantification of IFI between S1 and PPC-RL (S1↔PPC-A: 9 mice and 40 sessions and S1↔PPC-RL: 13 mice and 71 sessions; Wilcoxon signed-rank test; $^*P < 0.05$; $^{**}P < 0.01$; Supplementary Table 1).

texture-preferring sessions, S1 featured more texture neurons, weaker predictive texture encoding, slower texture encoding and slightly stronger bottom-up flow (Extended Data Fig. 10f–n). These differences suggest a flexible reconfiguration of S1 and PPC populations according to behavioral state.

Together, our results demonstrate that the dynamic interactions between S1 and PPC can shape sensory representation and govern the behavioral choices of mice (Fig. 7).

Discussion

We used a two-area two-photon microscope to study the interaction between a primary sensory area (S1) and the next-higher association area (PPC) during an auditory-cued texture discrimination task. We focused on cortico–cortical interactions underlying cross-modal predictive processing, by introducing tone and texture mismatches to induce conflicts between tone-based top-down texture predictions and bottom-up tactile input. When predictions dominated sensory inputs, as in trials in which mice decided based on tone instead of actual texture identity, we found that PPC-A encoded the expected texture, while in S1 both single-cell and population encoding of texture were disrupted. There was also stronger top-down information flow from PPC-A to S1. When tactile input dominated predictions, as reflected by texture-based choices, texture encoding in S1 and PPC remained unchanged, and bottom-up information flow from S1 to PPC-A was stronger (Fig. 7). Overall, our results provide evidence for a cortical implementation of predictive processing in the context of multisensory-driven decision-making.

Although predictive processing provides an attractive framework for understanding key brain functions, the specific neural circuits involved are yet to be fully understood. With experience, primary sensory cortices can develop specific predictions that impact stimulus responses—expected stimuli are suppressed and unexpected stimuli are amplified[6,7,36,37]. This occurs for both redundant unimodal stimulation[7,36,37] and multimodal stimulation where animals associate two stimuli[6,13]. Such predictions can be conveyed directly between sensory cortices[6], but also depend on long-range projections from higher areas[7,14,38]. Frontal higher areas have been extensively studied in contextual sensory processing[7,37,39], whereas posterior association areas received less attention. Frontal areas can modulate the activity in posterior areas of single sensory modalities through long-range projections[9,40]. Posterior association areas, in contrast, may integrate multiple sensory modalities and send processed information to primary as well as frontal areas. Here we provide evidence for such a process, as PPC-A formed an association between paired sensory stimuli and carried sufficient predictive information based on an initial tone to encode the expected texture.

How cortical areas communicate with each other and what information is exchanged during behavior are still open questions. Direct

https://doi.org/10.1038/s41593-023-01534-x

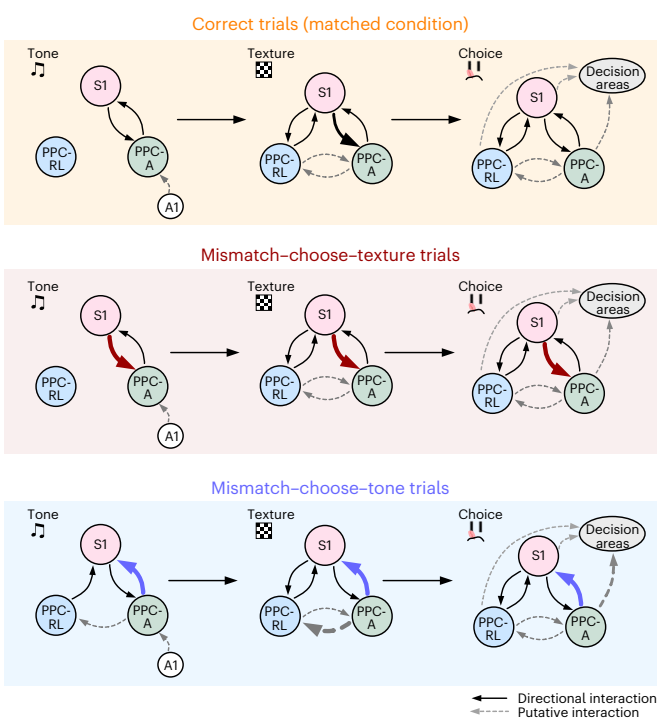

Fig. 7 | A model of S1, PPC-A and PPC-RL interactions during the behavioral task. a, In the correct trials, tone information is encoded in PPC-A, potentially through inputs from the auditory cortex (A1). PPC-A generates and communicates texture prediction with S1. During the texture presentation, S1 sends texture information to PPC-A, while all three areas are involved in the processing and transformation of texture information. The decision is formed through coordinated efforts from S1 and PPC. **b**, In mismatch–choose–texture trials, mice are in a state that attends more to S1 inputs. Texture information in S1 is sent to PPC-A, and a choice is made according to the actual texture. **c**, In mismatch–choose–tone trials, tone induces strong texture prediction in PPC-A, which is sent to S1 during the tone and texture windows, overwriting the actual texture information in S1. Choice is made according to the predicted texture. Solid arrows represent directional interactions between recorded areas, and dashed arrows represent putative interactions between pairs of areas that were not recorded simultaneously in this study.

projections from higher cortical areas to primary sensory areas can carry specific task-related information such as expected stimulus and reward[7,9,14], providing one mechanism for how top-down predictions affect responses in primary areas. Recent studies demonstrated that interactions between primary and higher areas usually occur in low-dimensional subspaces that do not necessarily align with the stimulus-encoding subspace[15,41], and that such interactions dynamically vary throughout stimulus presentation and behavioral tasks[16–19]. Our study adds to these findings by showing that the task-relevant variables are encoded in low-dimensional subspaces in S1 and PPC and that the dominance of either top-down or bottom-up processing corresponds to perceptual choices during the task. These findings are consistent with the predictive processing theory and reveal mechanisms underlying cortical information transformation and communication. Specifically, we observed that the disrupted texture encoding in S1 is accompanied by stronger top-down information flow from PPC. Our multimodal task design contributes to this observation because PPC is involved in multisensory processing[22,23,25,42] and therefore is well-positioned to develop cross-modal predictions. On the circuit level, such predictions could be implemented by disinhibition through top-down projections—in PPC as well as in primary areas, inhibitory interneurons have a key role in suppressing expected stimuli and augmenting unexpected stimuli[23,43,44]. Other brain areas such as the thalamus might be involved as well. Higher-order thalamic nuclei are interconnected with many cortical areas[20,45], providing another information routing station for processing of sensory conflicts by comparing top-down and bottom-up information.

In our task design, predictive processing is likely implemented through a multisensory integration process. We chose to use the term 'predictive processing' because it adequately describes the specific sensory association process, with two sensory modalities engaged sequentially such that a preceding tone is stably associated with a subsequent texture. Other forms of multisensory integration processes, for example, resolving conflicting simultaneous auditory and visual inputs that underlie conflicting reward rules[23,46], do not necessarily involve specific sensory predictions. Furthermore, predictive processing can be implemented through other mechanisms as well. For example, reward predictions[2,5,8] and unimodal sensory predictions (for example, mismatch negativity)[37,47] likely involve different neural circuits rather than the association cortex.

The composition and exact locations of rodent PPC and its subregions are still a topic of debate[22,26,48]. Historically, rodent PPC has been described as a part of higher visual areas, with PPC-RL largely overlapping with VISrl and PPC-A overlapping with VISam[33,48]. However, PPC receives not only visual input, but also extensive inputs from somatosensory, auditory and olfactory cortices, as well as higher cortical areas[22,49]. Most PPC studies so far defined PPC as a single area with varying coordinates, leading to contradictory results in some cases[23,50–52]. In our study, PPC-A and PPC-RL exhibited different task relevance, and both tone and texture neurons were more enriched toward the medial PPC. This coincides with the reports that PPC contains modality-specific subregions along the medial–lateral axis[26,49], but also suggests a functional reorganization of PPC through learned multisensory pairing[53]. PPC is not only a center for multisensory processing but also participates in decision-making[29,50,54,55]. Recent literature has shown that a topographic difference exists between the anterior and mediomedial regions of the PPC in encoding decisions[56]. Therefore, subregions in PPC likely serve as a continuum of intermediate routing stations of weighted sensory information flow toward frontal areas and top-down information back to sensory cortices. Further work is required to characterize in detail the specific roles of PPC subregions and their interactions.

Online content

Any methods, additional references, Nature Portfolio reporting summaries, source data, extended data, supplementary information, acknowledgements, peer review information; details of author contributions and competing interests; and statements of data and code availability are available at https://doi.org/10.1038/s41593-023-01534-x.

References

1. Keller, G. B. & Mrsic-Flogel, T. D. Predictive processing: a canonical cortical computation. *Neuron* **100**, 424–435 (2018).
2. Norman, K. J. et al. Post-error recruitment of frontal sensory cortical projections promotes attention in mice. *Neuron* **109**, 1202–1213 (2021).
3. Pakan, J. M. P., Currie, S. P., Fischer, L. & Rochefort, N. L. The impact of visual cues, reward, and motor feedback on the representation of behaviorally relevant spatial locations in primary visual cortex. *Cell Rep.* **24**, 2521–2528 (2018).
4. Schultz, W. & Dickinson, A. Neuronal coding of prediction errors. *Annu. Rev. Neurosci.* **23**, 473–500 (2000).
5. Starkweather, C. K., Gershman, S. J. & Uchida, N. The medial prefrontal cortex shapes dopamine reward prediction errors under state uncertainty. *Neuron* **98**, 616–629 (2018).
6. Garner, A. R. & Keller, G. B. A cortical circuit for audio-visual predictions. *Nat. Neurosci.* **25**, 98–105 (2021).

7. Fiser, A. et al. Experience-dependent spatial expectations in mouse visual cortex. *Nat. Neurosci.* **19**, 1658–1664 (2016).
8. Samuelsen, C. L., Gardner, M. P. H. & Fontanini, A. Effects of cue-triggered expectation on cortical processing of taste. *Neuron* **74**, 410–422 (2012).
9. Zhang, S. et al. Long-range and local circuits for top-down modulation of visual cortex processing. *Science* **345**, 660–665 (2014).
10. Libby, A. & Buschman, T. J. Rotational dynamics reduce interference between sensory and memory representations. *Nat. Neurosci.* **24**, 715–726 (2021).
11. Schmack, K., Bosc, M., Ott, T., Sturgill, J. F. & Kepecs, A. Striatal dopamine mediates hallucination-like perception in mice. *Science* **372**, eabf4740 (2021).
12. Corlett, P. R. et al. Hallucinations and strong priors. *Trends Cogn. Sci.* **23**, 114–127 (2019).
13. Gilday, O. D. & Mizrahi, A. Learning-induced odor modulation of neuronal activity in auditory cortex. *J. Neurosci.* **43**, 1375–1386 (2023).
14. Kwon, S. E., Yang, H., Minamisawa, G. & O'Connor, D. H. Sensory and decision-related activity propagate in a cortical feedback loop during touch perception. *Nat. Neurosci.* **19**, 1243–1249 (2016).
15. Semedo, J. D., Zandvakili, A., Machens, C. K., Yu, B. M. & Kohn, A. Cortical areas interact through a communication subspace. *Neuron* **102**, 249–259 (2019).
16. Semedo, J. D. et al. Feedforward and feedback interactions between visual cortical areas use different population activity patterns. *Nat. Commun.* **13**, 1099 (2022).
17. Ebrahimi, S. et al. Emergent reliability in sensory cortical coding and inter-area communication. *Nature* **605**, 713–721 (2022).
18. Javadzadeh, M. & Hofer, S. B. Dynamic causal communication channels between neocortical areas. *Neuron* **110**, 2470–2483 (2022).
19. Veuthey, T. L., Derosier, K., Kondapavulur, S. & Ganguly, K. Single-trial cross-area neural population dynamics during long-term skill learning. *Nat. Commun.* **11**, 4057 (2020).
20. Campo, A. T. et al. Feed-forward information and zero-lag synchronization in the sensory thalamocortical circuit are modulated during stimulus perception. *Proc. Natl Acad. Sci. USA* **116**, 7513–7522 (2019).
21. Chen, J. L. et al. Pathway-specific reorganization of projection neurons in somatosensory cortex during learning. *Nat. Neurosci.* **18**, 1101–1108 (2015).
22. Lyamzin, D. & Benucci, A. The mouse posterior parietal cortex: anatomy and functions. *Neurosci. Res.* **140**, 14–22 (2019).
23. Song, Y. H. et al. A neural circuit for auditory dominance over visual perception. *Neuron* **93**, 940–954 (2017).
24. Mohan, H. et al. Sensory representation of an auditory cued tactile stimulus in the posterior parietal cortex of the mouse. *Sci. Rep.* **8**, 7739 (2018).
25. Raposo, D., Kaufman, M. T. & Churchland, A. K. A category-free neural population supports evolving demands during decision-making. *Nat. Neurosci.* **17**, 1784–1792 (2014).
26. Gallero-Salas, Y. et al. Sensory and behavioral components of neocortical signal flow in discrimination tasks with short-term memory. *Neuron* **109**, 1–14 (2020).
27. Gilad, A. & Helmchen, F. Spatiotemporal refinement of signal flow through association cortex during learning. *Nat. Commun.* **11**, 1744 (2020).
28. Gilad, A., Gallero-Salas, Y., Groos, D. & Helmchen, F. Behavioral strategy determines frontal or posterior location of short-term memory in neocortex. *Neuron* **99**, 814–828 (2018).
29. Pho, G. N., Goard, M. J., Woodson, J., Crawford, B. & Sur, M. Task-dependent representations of stimulus and choice in mouse parietal cortex. *Nat. Commun.* **9**, 2596 (2018).
30. Rindner, D. J., Proddutur, A. & Lur, G. Cell-type-specific integration of feedforward and feedback synaptic inputs in the posterior parietal cortex. *Neuron* **110**, 3760–3773 (2022).
31. Park, I. M., Meister, M. L. R., Huk, A. C. & Pillow, J. W. Encoding and decoding in parietal cortex during sensorimotor decision-making. *Nat. Neurosci.* **17**, 1395–1403 (2014).
32. Chen, J. L., Voigt, F. F., Javadzadeh, M., Krueppel, R. & Helmchen, F. Long-range population dynamics of anatomically defined neocortical networks. *eLife* **5**, e14679 (2016).
33. Zhuang, J. et al. An extended retinotopic map of mouse cortex. *eLife* **6**, e18372 (2017).
34. Pachitariu, M. et al. Suite2p: beyond 10,000 neurons with standard two-photon microscopy. Preprint at *bioRxiv* https://doi.org/10.1101/061507 (2017).
35. Helmer, M. et al. On stability of canonical correlation analysis and partial least squares with application to brain-behavior associations. Preprint at *bioRxiv* https://doi.org/10.1101/2020.08.25.265546 (2023).
36. Audette, N. J., Zhou, W., La Chioma, A. & Schneider, D. M. Precise movement-based predictions in the mouse auditory cortex. *Curr. Biol.* **32**, 4925–4940 (2022).
37. Hamm, J. P., Shymkiv, Y., Han, S., Yang, W. & Yuste, R. Cortical ensembles selective for context. *Proc. Natl Acad. Sci. USA* **118**, e2026179118 (2021).
38. Parras, G. G. et al. Neurons along the auditory pathway exhibit a hierarchical organization of prediction error. *Nat. Commun.* **8**, 2148 (2017).
39. Hyman, J. M., Holroyd, C. B. & Seamans, J. K. A novel neural prediction error found in anterior cingulate cortex ensembles. *Neuron* **95**, 447–456 (2017).
40. Rodgers, C. C. & DeWeese, M. R. Neural correlates of task switching in prefrontal cortex and primary auditory cortex in a novel stimulus selection task for rodents. *Neuron* **82**, 1157–1170 (2014).
41. Srinath, R., Ruff, D. A. & Cohen, M. R. Attention improves information flow between neuronal populations without changing the communication subspace. *Curr. Biol.* **31**, 5299–5313 (2021).
42. Olcese, U., Iurilli, G. & Medini, P. Cellular and synaptic architecture of multisensory integration in the mouse neocortex. *Neuron* **79**, 579–593 (2013).
43. Hamm, J. P. & Yuste, R. Somatostatin interneurons control a key component of mismatch negativity in mouse visual cortex. *Cell Rep.* **16**, 597–604 (2016).
44. Schulz, A., Miehl, C., Berry, M. J. & Gjorgjieva, J. The generation of cortical novelty responses through inhibitory plasticity. *eLife* **10**, e65309 (2021).
45. Harris, J. A. et al. Hierarchical organization of cortical and thalamic connectivity. *Nature* **575**, 195–202 (2019).
46. Deneux, T. et al. Context-dependent signaling of coincident auditory and visual events in primary visual cortex. *eLife* **8**, e44006 (2019).
47. Van Derveer, A. B., Ross, J. M. & Hamm, J. P. Robust multisensory deviance detection in the mouse parietal associative area. *Curr. Biol.* **33**, 3969–3976 (2023).
48. Gilissen, S. R. J., Farrow, K., Bonin, V. & Arckens, L. Reconsidering the border between the visual and posterior parietal cortex of mice. *Cereb. Cortex* **31**, 1675–1692 (2021).
49. Zingg, B. et al. Neural networks of the mouse neocortex. *Cell* **156**, 1096–1111 (2014).
50. Goard, M. J., Pho, G. N., Woodson, J. & Sur, M. Distinct roles of visual, parietal, and frontal motor cortices in memory-guided sensorimotor decisions. *eLife* **5**, e13764 (2016).

51. Zhong, L. et al. Causal contributions of parietal cortex to perceptual decision-making during stimulus categorization. *Nat. Neurosci.* **22**, 963–973 (2019).
52. Oude Lohuis, M. N., Marchesi, P., Pennartz, C. M. A. & Olcese, U. Functional (ir)relevance of posterior parietal cortex during audiovisual change detection. *J. Neurosci.* **42**, 5229–5245 (2022).
53. Driscoll, L. N., Pettit, N. L., Minderer, M., Chettih, S. N. & Harvey, C. D. Dynamic reorganization of neuronal activity patterns in parietal cortex. *Cell* **170**, 986–999 (2017).
54. Morcos, A. S. & Harvey, C. D. History-dependent variability in population dynamics during evidence accumulation in cortex. *Nat. Neurosci.* **19**, 1672–1681 (2016).
55. Harvey, C. D., Coen, P. & Tank, D. W. Choice-specific sequences in parietal cortex during a virtual-navigation decision task. *Nature* **484**, 62–68 (2012).
56. Kira, S., Safaai, H., Morcos, A. S., Panzeri, S. & Harvey, C. D. A distributed and efficient population code of mixed selectivity neurons for flexible navigation decisions. *Nat. Commun.* **14**, 2121 (2023).

Methods

All procedures of animal experimentation were carried out according to the guidelines of the Veterinary Office of Switzerland and following approval by the Cantonal Veterinary Office in Zurich (licenses 234/2018, 211/2018).

Mice and dataset

Mice were housed on a reversed 12-h light/12-h dark cycle at an ambient temperature of between 21 °C and 23 °C and humidity between 55% and 60%. A total of 16 mice were included in this study. Mice were one of the following strains: RasGRF2a-dCre;CamK2a-tTA;TITL-GCaMP6f (M10, M11, M12, M25, M26, M28, M29, M33, M34, M35), GP5.17(C57BL/6J-Tg(Thy1-GCaMP6f)GP5.17Dkim/J) (M14 and M15; Jackson Laboratory, 025393), Snap25-IRES2-Cre-D;CamK2a-tTA;TITL-GCaMP6f (M17) and RasGRF2a-dCre;tTA2-GCaMP6f (M30, M38, M40). All transgenic strains express GCaMP6f in layer 2/3 pyramidal neurons of the neocortex. Both sexes were included in this study (male: M10, M14, M15, M25, M26, M30, M33, M34, M35; female: M11, M12, M13, M17, M28, M29, M38, M40). All mice were adults (12–16 weeks old) when the experiment started. Of the 16 mice, S1–PPC_A imaging was performed on 9 mice (M25, M26, M28, M29, M30, M33, M34, M35, M40) and S1–PPC_{RL} imaging was performed on 14 mice (M10, M11, M12, M14, M17, M25, M26, M28, M29, M30, M33, M34, M35, M40). Two mice (M15 and M38) were only included in behavioral studies but not in the neuronal data analysis due to the decayed cranial window quality. One mouse (M17) was removed from cross-area analysis due to decayed S1 imaging quality from lateral skull bone growth under the cranial window. Mice were 2.5–4 months old at the beginning of behavior training and 3–5 months old at the time of the experiment.

Surgical procedures

A craniotomy was performed on all mice over S1 and PPC in the left hemisphere. Mice were anesthetized with 2% isoflurane mixed with oxygen, and body temperature was maintained at 37 °C. After analgesia treatment (Metacam, 5 mg kg^{-1}, s.c.; lidocaine gel over the skull skin), the skull was exposed, and a 4-mm round cranial window was made with a dental drill and covered with glass coverslip using dental cement (Tetric EvoFlow). A light-weighted head-bar was fixed on the skull using dental cement. After the surgery, animals were continually monitored for at least 3 d and treated with analgesics (Metacam, 5 mg kg^{-1}, subcutaneous). For strains that expressed destabilized Cre (dCre), we induced stable GCaMP6f expression by administering trimethoprim (TMP; Sigma-Aldrich, T7883). TMP was reconstituted in dimethyl sulfoxide (Sigma-Aldrich, 34869) at a saturation level of 100 mg ml^{-1} and intraperitoneally injected (150 mg TMP per gram body weight; 29 g needle) at least 1 week before imaging commenced.

Behavior training

Mice were allowed to recover for at least 1 week before behavior training started. Mice were first accustomed to the hands of the experimenter at the home cage for several days until showing no sign of stress and then accustomed to head fixation. Then, mice were put under water scheduling and were introduced to the behavior setup. During the first two to three sessions, mice were given a sugar water reward from one of the two lick ports after the choice tone (two beeps at 3 kHz of 50-ms duration with 50-ms interval). Once they learned to lick after the choice tone to obtain the water reward, we introduced the textures. Textures were followed by reward delivery on the corresponding lick port upon licking, and licks on the wrong port did not result in punishment or trial abort. This stage lasted for one to two sessions. Once mice were accustomed to the trial structure, we started formal training.

Behavior training was carried out using custom-written LabView software. Each trial started with one of two distinct auditory tones (10 kHz or 18 kHz, six repetitions, 50-ms duration and 50-ms intervals). One second after tone onset, the presentation of one of two distinct textures followed (sandpaper, P100 versus P1200 for M10–17, P280 versus P800 for M25–40). A rotary motor 'swung' the texture onto the whisker pad from the top. The texture was presented for 1 s and then moved away from the mouse with a linear motor stage. At the end of the texture window, the choice window started, indicated by the choice tone described above. The choice window lasted for up to 2 s. As soon as mice licked during the choice window, the choice window was terminated and the reward window started. If mice chose the correct lick port, a small water reward was delivered (~4 µl sugar water); wrong choices were not punished. The intertrial interval was randomly distributed between 4 and 8 s.

During training, when a mouse made incorrect choices, the same tone–texture stimulus pair was presented again in the following trial until the mouse chose correctly. This 'repeat incorrect' strategy facilitates learning and prevents the mice from forming a bias toward one of the two lick ports. If the mouse disengages from licking, in 10% of these miss trials, the reward was delivered after the choice window to motivate the mouse. Each day, the training lasted as long as the mouse was actively engaged in the task, typically 200–400 trials. Training was done once per day, 5–6 d per week. Weight, health and water intake were monitored daily. All training was performed in the dark and monitored through a behavior camera with a small infrared light source. Mice were considered experts when they reached 75% correct performance for three sessions. Among all mice, three mice showed unstable behavior, with relatively high fluctuations of the within-session performance (Extended Data Fig. 1a); however, they all showed clear signs of learning, reaching subsession performance peaks above expert level for consecutive days. We attributed the unstable behavior to environmental stress; in particular, the training of M40 coincided with construction work in the animal facility, resulting in a longer training duration.

Mismatched trial design

After mice became stable experts, we started introducing mismatched trials. In these sessions, the first 20–30 trials were with matched stimuli (without mismatch) and only afterward mismatched trials were randomly presented in 10–30% of the trials. To avoid confusion for mice and prevent relearning of new rules, we kept the repeat incorrect strategy throughout these sessions for matched trials, reinforcing the learned rules. Because the task is mostly a texture-dependent task ('Results'; Fig. 1 and Extended Data Fig. 1), we rewarded according to the tone in mismatched trials, to encourage mice to pay attention to the tone and generate more mismatch–choose–tone response.

Single sensory modality experiments

Tone-only and texture-only sessions were done at the end of the experiment after mice completed all mismatched sessions (7–12 sessions). In tone-only sessions, trials started with a 1-s auditory tone, as for the matched pairing condition. Afterward, the rotary motor carrying the texture swung in, generating the same motor noise, but stopped above the whisker pad of mice. Therefore, the texture was 'presented' above the mice, out of reach for their whiskers. Choice window, reward window and intertrial interval were the same as in matched condition. In texture-only sessions, the tone before the texture presentation was omitted. Trial started with a 1-s window with no sensory stimulus, followed by normal texture presentation, and then choice and reward windows. These single-modality sessions were typically restricted to 100–150 trials to prevent relearning.

After the single-modality experiments, we trimmed the whiskers of the mice and conducted another texture-only session. This session served as a control experiment to exclude the possibility that mice relied on other environmental cues (visual, olfactory and so on) to perform the task.

Behavior monitoring

Face and body movements as well as the pupil diameter of the mice were monitored and recorded using a complementary metal–oxide semiconductor (CMOS) infrared-sensitive camera (Basler acA1440-220um). A small 940-nm infrared light-emitting diode (LED) was positioned in front of the mice to illuminate their face and body. Because mice were in complete darkness, their pupils were dilated by default. To monitor the pupil diameter with a larger dynamic range, we restrained the pupil by carefully positioning a small ultraviolet LED (385 nm; Thorlabs, LED385L) close to the eye contralateral to the texture presentation. Trial-related behavior was recorded at 50 Hz, simultaneously with calcium imaging, triggered by each trial start. Licking was recorded throughout tone, texture and choice windows and was estimated based on the event rate from the capacitive lick sensor sampled at 100 Hz.

To extract body and face movements, we manually selected two regions of interest (ROIs), one on the whisker pad and the other on the forelimb and chest region. Movement was calculated as frame-to-frame variation by computing $(1-\mathrm{corr}(f_t, f_{t+1}))$, where $\mathrm{corr}(f_t, f_{t+1})$ denotes the frame-to-frame correlation of the ROI. We tracked the pupil diameter using a custom MATLAB script. First, we manually selected an ROI over the eye region and binarized the pupil (pupil was bright due to two-photon illumination of the cortex at 920 nm). Then, pupil diameter was estimated by fitting the binary region to an ellipse. Body and face movements, as well as pupil diameter, were smoothed with a median filter of a 200-ms width.

Sensory mapping

To determine the exact locations of S1 and PPC, we performed widefield sensory mapping on all the mice before the two-photon imaging sessions started, following a previously described procedure[26]. Mice were lightly anesthetized under 1% isoflurane and kept at 37 °C. The following three types of sensory stimuli were delivered: visual, whisker and hindlimb. For visual stimulation, a small blue LED was positioned close to the eye contralateral to the cranial window and a brief 200-ms flash was presented, followed by recovery time of 10 s. For whisker and hindlimb stimulation, a loud speaker-coupled vibrating bar was used to induce vibrating touches of the whiskers and hindlimb paw (20 Hz for 2 s) on the side contralateral to the cranial window. Each stimulus modality was repeated 30 times.

Widefield imaging was simultaneously performed through the cranial window. A blue LED light source (Thorlabs, M470L3) was used for the excitation of GCaMP6f, together with an excitation filter (480/40 nm; BrightLine HC). The excitation light was directed through a dichroic mirror (510 nm; AHF; Beamsplitter T510LPXRXT) to a 4× objective (Thorlabs, TL4X-SAP, 0.2 NA). Emission light was filtered (emission filter 529/24 nm, BrightLine HC) and passed through the dichroic mirror to separate emission light with excitation light, then through a tube lens (Thorlabs, TTL100-A) onto a sensitive CMOS camera (Hamamatsu Orca Flash 4.0).

To obtain a more precise location of PPC-RL and PPC-A, we further generated a retinotopic map through visual field sign mapping, following a previously described procedure[33]. Briefly, a drifting spherically corrected checkerboard visual stimulus was presented on an LED screen (Adafruit Qualia 9.7′ DisplayPort Monitor, 2,048 × 1,536 resolution) across the visual field of the mice at 0.043–0.048 Hz. The stimulus sequence consisted of four cardinal directions, each presented with ten repetitions. The screen was positioned in front of the eye contralateral to the cranial window, such that the stimulus covered retinotopic locations from approximately −20° to +30° in altitude and −10° to +90° in azimuth. The retinotopic map was calculated using a previously reported analysis pipeline[33]. The final location of S1, PPC-A and PPC-RL was determined by optimally aligning the sensory map and retinotopic map together to the Allen Mouse Common Coordinate[45].

Two-area two-photon imaging

Two-area two-photon imaging was performed using a custom-built microscope that has been previously reported[32]. The simultaneous two-area imaging was implemented through a temporal multiplexing technique, where the laser pulse train from a Ti:sapphire laser (Mai Tai HP DeepSee; Spectra-Physics) was split into two temporally interleaved copies, each directed through an independently movable unit to a separate field of view (FOV). Each beam path was equipped with an electrically tunable lens (Optotune, EL-10-30-C) to enable rapid focal changes for imaging multiple depths. Imaging was done at 920-nm excitation with a green emission filter (510/42 nm bandpass). A 16× objective was used (Nikon, N16XLWD, 0.8 NA). The microscope was controlled by a custom-written software Scope (http://sourceforge.net). Calcium imaging was acquired at three different depths in layer 2/3, separated by 40–50 µm. The FOV size was ~450 × 500 µm, at a resolution of ~370 × 256 pixels. The volume rate was typically ~9.32 Hz for two areas and three imaging depths per area. Laser power was adjusted for each plane, at 40–70 mW under the objective. For each mouse, the FOV positions and/or depths were slightly adjusted for each imaging session to cover different neuronal populations in S1 and PPC. Imaging was triggered by the start of each trial, and the image acquisition finished 0.5 s before the end of the intertrial interval (that is, the start of the next trial). During the duration of the experiment, most mice maintained a clear window with good imaging quality. The number of imaging sessions for each mouse is as follows: for S1–$\mathrm{PPC_A}$ imaging, the number of sessions was 3, 4, 5, 5, 4, 4, 7, 4 and 4 for M25, M26, M28, M29, M30, M33, M34, M35 and M40, respectively. For S1–$\mathrm{PPC_{RL}}$ imaging, the number of sessions was 10, 9, 10, 2, 1, 8, 5, 4, 8, 5, 3, 4, 4 and 3 for M10, M11, M12, M14, M17, M25, M26, M28, M29, M30, M33, M34, M35 and M40, respectively. Note that the number of PPC-RL sessions was higher for M10, M11 and M12 due to a lower percentage of mismatched trials (~10% mismatched trials).

Processing of two-photon imaging data

We used Suite2p to extract neuronal traces[34]. This pipeline includes a rigid motion correction on the raw data, a model-based background subtraction, a neuron-identification algorithm, fluorescence extraction and a neuron classifier. Raw fluorescence and neuropil traces were extracted from identified neurons, and neuropil-corrected traces were obtained. A deconvolution algorithm was applied to the corrected fluorescence traces to estimate the spike rate of neurons (in arbitrary units). Spike rate was further normalized by their baseline F0. We tuned the neuron classifier in the above pipeline to identify potential neurons, and we further manually curated each dataset to discard non-neuronal structures or low-quality ROIs. All neuronal data analysis was performed using deconvolved spike rates.

To exclude redundant neurons due to fluorescence signal bleed-through between two areas or between two neighboring depths, we removed neurons that were highly correlated to neighboring neurons, using similar criteria as previously described[57]. We defined potential duplicated neuron pairs as follows: (1) spike rate correlation above 0.5; (2) lateral distance between centroids below 5 µm regardless of depths; (3) appeared in adjacent imaging depths in the same imaging area (signal bleed-through in the same area from adjacent imaging planes) or appeared in the same imaging depths in different imaging areas (signal bleed-through across areas from the same imaging plane). In these duplicated neuron pairs, we kept the neuron with the highest average fluorescence level and discarded the one with less fluorescence.

Due to the variable length of the choice window, we defined the choice window as the 0.5-s time period before the lick that triggered the reward window (equivalent to the 0.5-s period before the reward window). We resampled all behavior data to match the calcium imaging rate. Due to slight differences in imaging rate (caused by slightly different pixel numbers), when combining datasets together, we resampled

all datasets to a standard 10 Hz rate. These procedures were applied before all the analyses below.

Responsive neuron analysis

To identify neurons that are responsive to different task phases, we tested the activity level of individual neurons across task windows, for T_{tone}, $T_{texture}$, T_{choice} and T_{reward}. We first denoised the deconvolved spike rates by a small Gaussian window (three frames, sigma = 1); then, for each neuron n_i and each task window T_j, we compared its average activity within the window and generated a baseline distribution by randomly sampling the same number of frames outside of window T_j and computing average activity, for 100 times. If the activity of neuron n_i in T_j was significantly higher than outside of T_j, determined by a one-tailed Wilcoxon rank-sum test ($P < 0.05$), then we define neuron n_i as responsive in task window T_j.

To identify neurons that are discriminative for a specific task variable (tone, texture, choice and reward), we compared the activity of responsive neurons as defined above for the different values of the task variables. For each task variable (for example, texture), there are two potential values s_1 and s_2 (for example, texture 1 and texture 2). We compared the average activity of each neuron within the corresponding task window (texture window in this example) between s_1 trials and s_2 trials, using the Wilcoxon rank-sum test. If the neuronal activity was significantly higher ($P < 0.05$) in s_1 trials, then the neuron was defined as a discriminative neuron with a preference for s_1. We performed this procedure for all four task variables. Responsive and discriminative neurons identified with this method are nonrandom, as no significant neurons were identified in shuffled data, where the activity of individual neurons was randomized within sessions. The relatively low percentage of discriminative neurons is due to several factors, which are as follows: (1) we calculate the percentage using all detected neurons from the entire imaged population (several hundreds of neurons using our custom microscope); (2) we defined discriminative neurons as a subset of responsive neurons, that is, they were required to have increased firing rate during the specific task phase; (3) we used two relatively similar textures P280 and P800 in our task design.

Responsive neuron analysis with GLM

To further dissect texture- and choice-related activity during texture presentation, we built Gaussian GLM (with identity link function) with two regressors (texture and choice) to predict the average texture window activity of each neuron, following a previously published procedure[58]. Each regressor contains the following two values: −1 (texture 2 and choice 2) and 1 (texture 1 and choice 1). For each neuron, we trained a full model using all regressors with twofold cross-validation. To avoid overfitting, we applied ridge regularization with a lambda penalty of 0.1. We quantified model performance by computing the correlation value between the predicted activity and real activity. To identify the contribution of each regressor, we shuffled each regressor vector 100 times while maintaining the rest unchanged and fitted the model as above. We considered a neuron to be texture- or choice-responsive if the correlation value of the full model is 1.96 s.d. away from the shuffled distribution. Among these neurons, discriminative neurons were identified as described in the section above ('Responsive neuron analysis').

Decoder analysis

We trained the following four types of linear SVM decoders: tone, texture, choice and reward decoders, respectively. Similar to the responsive neuron analysis, each type of decoder was trained with two class labels (for example, texture 1 versus texture 2), using frame-concatenated spike rate data from the corresponding task window (for example, texture window). A separate decoder was trained for each imaging session and each area (S1, PPC-A and PPC-RL), due to different imaging populations. Only matched pairing trials were used for training decoders.

For each imaging session, we randomly divided all the matched pairing trials into ten subsets. We trained ten decoders by excluding one subset at one time; therefore, each decoder was trained on 90% of the training set. To avoid overfitting, we regularized the SVM coefficients with ridge (L2) penalty. The regularization term was cross-validated in a log space of ten parameters from 10^{-5} to 10^{1}. To avoid overfitting due to unbalanced class number, we also implemented a misclassification cost that is inversely correlated with the total number of each class. The projection strength of each trial was calculated using the decoder that was not trained using this trial. The projection strength at time t of a trial was defined as the dot product between the decoder coefficient (without the constant term) and the population spike rate vector at t. Shuffled controls were generated by randomizing the neuron identities in the dataset and applying the decoders to shuffled data. To evaluate the decoder performance, the receiver operating characteristic curve and the area under the curve (AUC) were calculated using standard approaches, and the discrimination index (DI) was defined as (AUC-0.5) × 2. DI = 0 represents chance level, and DI = 1 represents perfect classification performance.

CCA analysis

To measure the optimal population correlation between cortical areas, we applied a previously reported method, the CCA[16,19]. CCA identifies pairs of dimensions from the imaged neuronal populations in the two cortical areas, such that the correlation between the projected activities onto the dimension is maximized. Given the activity of two neuronal populations, a $n_x \times t$ matrix X from area 1 and a $n_y \times t$ matrix Y, where t is the number of time points and n_x and n_y are the number of neurons in each area, CCA identifies in total $\min(n_x, n_y)$ pairs of dimensions, and the projection correlation of these dimensions decreases from the first to last. Similar to PCA, CCA finds a set of projection axes for each area; the difference is that PCA aims at maximizing the variance explained by top axes from X and Y, independently, while CCA aims at maximizing the projection correlation between the activity matrices X and Y.

CCA requires a sufficient amount of samples to generate stable solutions[35]. In our experiments, we typically imaged 200–300 neurons in each area, and we recorded 200–400 trials per session. A previous study using simulated datasets has shown that ~50 samples per variable are required to generate a stable solution[35]. To ensure such a condition is met, we first performed PCA to reduce the dimensionality (number of variables) per area, keeping the first 30 principal components (PCs). Overall, the top 30 PCs captured a substantial part of the variance in the dataset (variance explained by 30 PCs: S1, 55.0 ± 1.2; PPC-A, 59.9 ± 1.4; PPC-RL, 53.7 ± 1.5 (mean ± s.e.m.)). We aimed at generating a separate CCA model at each time point over the trial time; to further increase the sample number and to avoid outliers as well as to introduce certain temporal smoothness, we took a sliding time window of 0.5 s (five frames) for training. Using a smaller time window (0.3 s) yielded more noisy but overall similar results (Supplementary Fig. 1). For each time window, we randomly divided the data into ten subsets and generated ten models by leaving one subset out each time. The final correlation is computed as the average from the ten models.

The stimuli in the task result in the co-activation of neurons caused by common inputs. As we were interested in the intrinsic interaction between cortical areas, we analyzed the residual activity by subtracting stimulus-triggered averages of PCs, from eight types of stimulus combinations (two tones, two textures and two choices). Additionally, we observed performance variability within individual sessions, and to ensure that we were analyzing trials during which mice were engaged in the task, we divided each session into subsessions of 20 trials and used only the subsessions with performance rates above 75% for analysis. For tone-only and texture-only conditions, we kept the last 50 trials (of 100–150 trials) when the performance had stabilized. This resulted in 40–400 trials for each session.

Because we reduced the dimensionality of each population to its top 30 PCs, the CCA model generated 30 dimensions with descending interareal correlation. To determine the number of significant dimensions, we shuffled the trial correspondence between the two areas 100 times and computed the CCA correlations in the same way as above. The significance threshold was defined as mean + 3 s.d. of the highest shuffled correlation. CCA dimensions with correlations exceeding the significance threshold were regarded as significant dimensions. Overall, we observed one to two significant dimensions across datasets and time points; therefore, we focused on the first CCA dimension for analysis.

To analyze top-down and bottom-up interactions, we introduced a negative lag of up to 0.5 s with 0.1-s increment to each area, separately. For top-down interaction, we introduced a negative lag to the PPC data (PPC-A or PPC-RL); for bottom-up interaction, we introduced a negative lag to the S1 data. At each lag, we generated a CCA model, consisting of two separate loading matrices corresponding to the two areas. Then, for each trial type (correct, mismatch–choose–texture and mismatch–choose–tone), we computed the projection correlation of all trials in this trial type. This approach avoided the potential instability of training the CCA model for each trial type, which does not guarantee enough sample numbers. From here, the lagged correlation map was slightly smoothed with a small Gaussian kernel (three frames, sigma = 1) to reduce noise between temporally consecutive models, and top-down and bottom-up interaction strengths were computed as the average CCA correlations across 0.3-s lags. Using different lags (0.1 s and 0.5 s) gave similar results as shown in Fig. 6. The direction and strength of information were quantified as information flow index (IFI), defined as (bottom-up − top-down)/(bottom-up + top-down). IFI is bounded between −1 and 1. Values close to −1 represent top-down dominant information, values close to 1 represent bottom-up dominant information and values close to 0 represent simultaneous or no information transfer.

Pearson correlation analysis

To verify our results of CCA, we also calculated population correlations using Pearson correlation instead of CCA. The imaging data were processed in the same way as for CCA analysis, but population correlation was computed as the Pearson correlation between the flattened residual matrices of the two areas. Shuffled correlation was computed from trial-shuffled residual matrices. Unlike CCA, which found a positive correlation in all cases, Pearson correlation resulted in negative values in some cases. For the calculation of IFI, we first normalized the lagged correlation map to be between 0 and 1, then calculated IFI for each trial type.

Statistics and reproducibility

All statistical analysis was done in MATLAB. In general, the Wilcoxon signed-rank test was used for paired samples and the Wilcoxon rank-sum test was used for nonpaired samples. No normality test was performed because these tests do not assume normality. Equal variance was assumed but not formally tested. Two-sided tests were performed unless otherwise indicated. No statistical methods were used to predetermine sample sizes, but our sample sizes are similar to those reported in previous publications[10,26,59]. Error bars represent mean ± s.e.m. Boxplots indicate the median (center line), 25% and 75% quartiles (box limits) and 1.5× interquartile range (whiskers). The exact *P* values are included in Supplementary Table 1. Mice were randomly assigned to imaging conditions (S1-PPC$_A$ or S1-PPC$_{RL}$ imaging) on each day. Stimulus presentation during imaging was fully randomized. Data collection and analysis were not performed blind to the conditions of the experiments.

Reporting summary

Further information on research design is available in the Nature Portfolio Reporting Summary linked to this article.

Data availability

A subset of the data is available at a Zenodo repository[60] due to space limitations. The full dataset is available from the corresponding authors upon request. Source data are provided with this paper.

Code availability

Example data processing and analysis code is available at a Zenodo repository[60].

References

57. Han, S., Yang, W. & Yuste, R. Two-color volumetric imaging of neuronal activity of cortical columns. *Cell Rep.* **27**, 2229–2240 (2019).
58. Buetfering, C. et al. Behaviorally relevant decision coding in primary somatosensory cortex neurons. *Nat. Neurosci.* **25**, 1225–1236 (2022).
59. Chen, J. L., Carta, S., Soldado-Magraner, J., Schneider, B. L. & Helmchen, F. Behaviour-dependent recruitment of long-range projection neurons in somatosensory cortex. *Nature* **499**, 336–340 (2013).
60. Han, S. Behavior-relevant top-down cross-modal predictions in mouse neocortex. *Zenodo* https://doi.org/10.5281/zenodo.10078711 (2023).

Acknowledgements

We thank P. Bethge for managing transgenic mouse lines, F. Voigt and H. Kasper for help with optics, and M. Wieckhorst for the behavior training software. We also thank C. Lewis, J. Chen and J. Hamm for their feedback on the paper. This work was supported by a Sinergia grant from the Swiss National Science Foundation (CRSII5_180316 to F.H.) and a Forschungskredit grant from University of Zurich (K-41220-07-01 to S.H.). F.H. received funding from the University Research Priority Program (URPP) 'Adaptive Brain Circuits in Development and Learning' (AdaBD).

Author contributions

S.H. performed the experiments and analyzed the data. S.H. and F.H. conceived the study, designed the experiments and wrote the paper.

Competing interests

The authors declare no competing interests.

Additional information

Extended data is available for this paper at https://doi.org/10.1038/s41593-023-01534-x.

Supplementary information The online version contains supplementary material available at https://doi.org/10.1038/s41593-023-01534-x.

Correspondence and requests for materials should be addressed to Shuting Han or Fritjof Helmchen.

Peer review information *Nature Neuroscience* thanks Seung-Hee Lee and the other, anonymous, reviewer(s) for their contribution to the peer review of this work.

https://doi.org/10.1038/s41593-023-01534-x

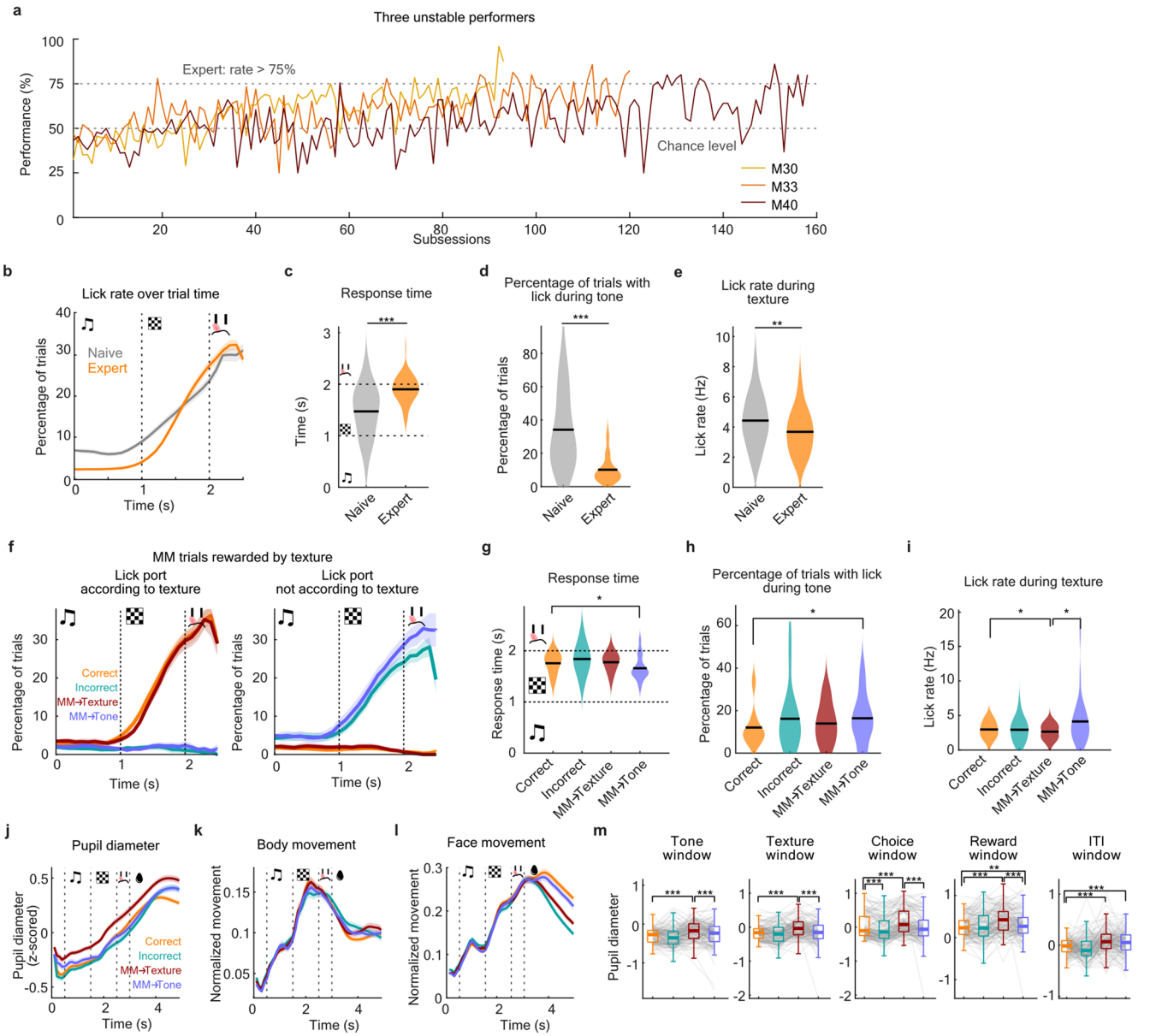

Extended Data Fig. 1 | Additional behavior analysis. (**a**) Each day, all the trials were split into 2–5 subsessions of 100–150 trials. Three unstable performer mice that did not reach expert threshold in daily average all showed expert performance in individual subsessions. (**b**) Lick rate over time for naïve and expert mice. (**c**) Response time of naive (performance<55%, 16 mice, 80 sessions) and expert mice (performance>75%, 13 mice, 74 sessions). (**d**) Percentage of trials with lick during tone on the lick port of final choice for naïve and expert mice. (**e**) Lick rate during texture for naïve and expert mice. (**f**) Lick probability over trial time on the lick ports according to texture identity (left) or the opposite lick port (right), during sessions where mismatched trials were rewarded according to texture (same for **g**–**i**). (**g**) Response time for different trial types. Mismatch-choose-tone condition shows a shorter response time overall. (**h**) Percentage of trials in each session, in which licks on the final choice spout were recorded during tone presentation. (**i**) Lick rate during texture presentation for different trial types. (**j**) Z-scored pupil diameter in different trial types. (**k**) Body movement (normalized between 0 and 1 within each day) across trial types. (**l**) Face movement (normalized between 0 and 1 within each day) across trial types. (**m**) Statistics of pupil diameter across trial time. ((**b**–**e**): Wilcoxon rank-sum test, (**f**–**m**): Wilcoxon signed-rank test; (**a**–**e**, **j**–**m**) mice and session numbers are the same as Fig. 1; (**f**–**i**) 6 mice, 17 sessions; $^{*}P < 0.05$; $^{**}P < 0.01$; $^{***}P < 0.001$; Supplementary Table 1).

https://doi.org/10.1038/s41593-023-01534-x

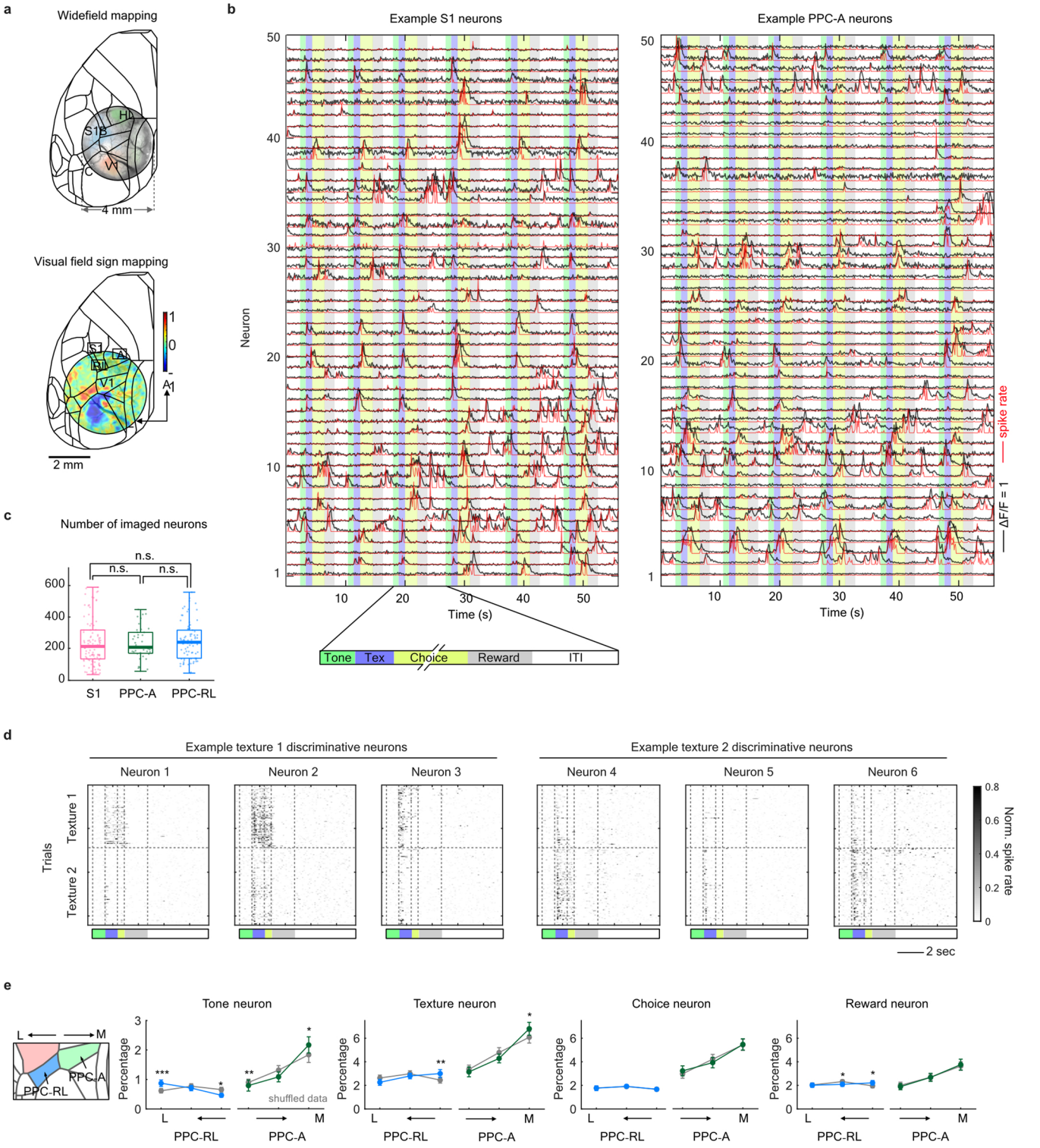

Extended Data Fig. 2 | Additional information on imaging and task-tuned neurons. (**a**) The locations of S1, PPC-A and PPC-RL were determined by widefield sensory mapping using whisker, visual and hindlimb stimulation (top) under light anesthesia, as well as visual field sign mapping (bottom). (**b**) Example ΔF/F (black) and deconvolved spike rate (red) of two simultaneously imaged S1 and PPC-A populations. Due to space limitation, only 50 neurons are shown for each area. Colored stripes in the background indicate task windows. Some neurons were silent in the example time period shown in the plot. (**c**) Number of imaged neurons for each area are not significantly different. (**d**) Example single trial activities of texture discriminative neurons. Three example neurons from the same imaging session are shown for each texture preference; choice window was resampled to be the 0.5-s window before the reward window. Trial structure and color code are the same as in (**b**). (**e**) Distribution of PPC task-responsive neurons along the medial-lateral (M-L) axis. Task-responsive neurons in PPC-RL and PPC-A were assigned to 3 spatial bins along the M-L axis. Percentage was calculated using the number of total neurons in each area. Shuffled data are represented in gray, where the neurons that the match number of responsive neurons were randomly drawn from the population. (S1: 14 mice, 118 sessions; PPC-RL: 14 mice, 78 sessions; PPC-A: 9 mice, 40 sessions; Wilcoxon signed-rank test; $^{*}P < 0.05$; $^{**}P < 0.01$; $^{***}P < 0.001$; Supplementary Table 1).

https://doi.org/10.1038/s41593-023-01534-x

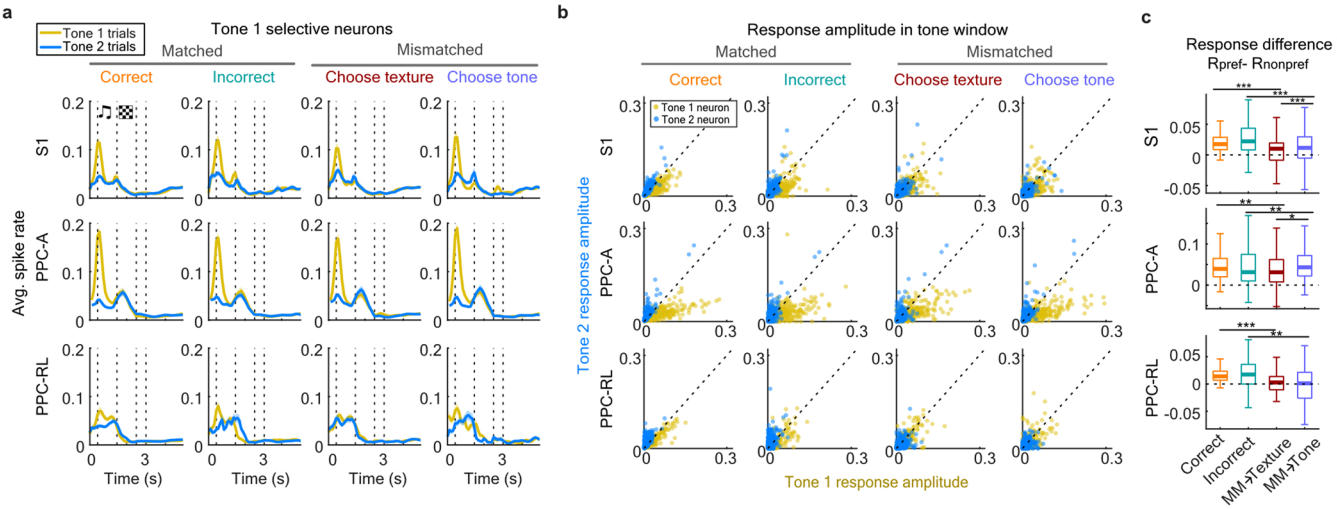

Extended Data Fig. 3 | Response amplitude of tone-discriminative neurons. (**a**) Averaged normalized spike rate of tone 1 discriminative neurons in S1, PPC-RL and PPC-A, in matched and mismatched trials. The spike rate of each neuron was normalized to be between 0 and 1 within each session. (**b**) The mean response amplitudes of all tone discriminative neurons in the tone window, across areas and trial types. (**c**) Selectivity index of tone discriminative neurons during tone window, in different trial types. Significance level was determined from shuffled data where the trial labels were shuffled. (S1: 119 neurons; PPC-A: 170 neurons; PPC-RL: 94 neurons; Wilcoxon rank-sum test; $^{*}P < 0.05$; $^{**}P < 0.01$; $^{***}P < 0.001$; Supplementary Table 1).

https://doi.org/10.1038/s41593-023-01534-x

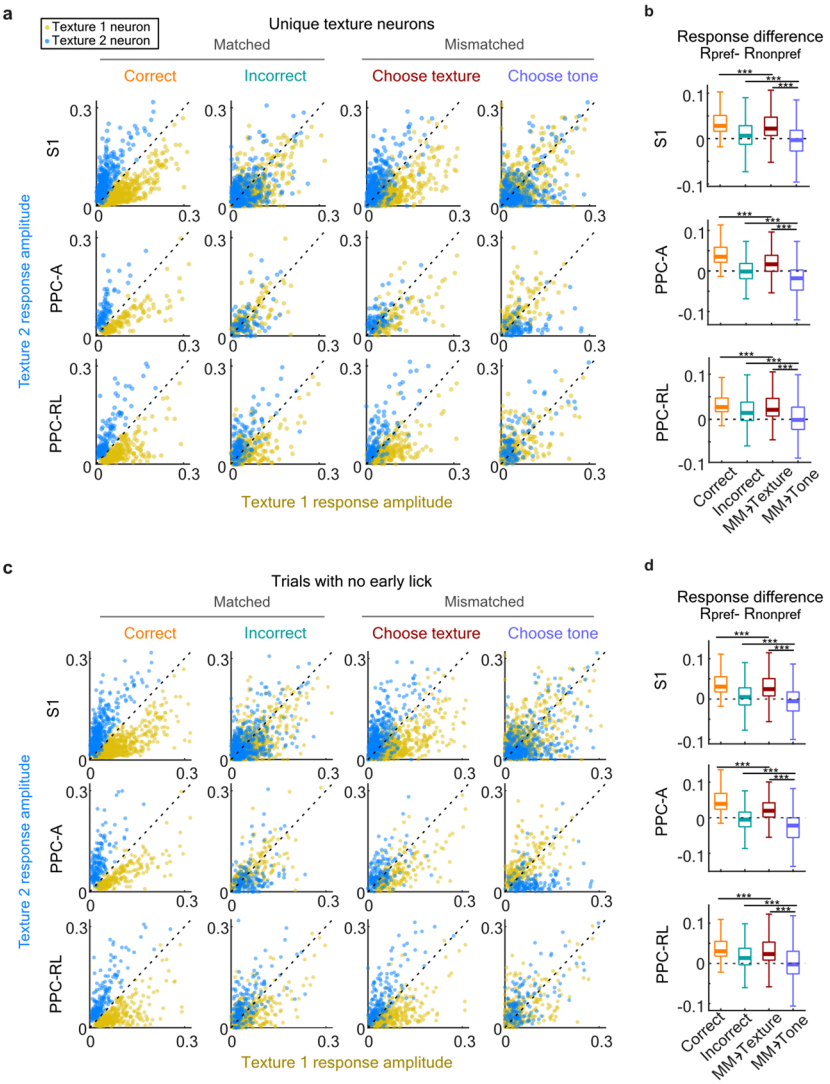

Extended Data Fig. 4 | Response amplitude of texture-discriminative neurons without the influence of choice. (**a**) The mean texture response amplitudes of all texture discriminative neurons that were not choice-responsive, across areas and trial types. Each dot represents the response of one neuron in one imaging session. (**b**) Selectivity index of texture discriminative neurons during texture window, in different trial types. Selectivity index was calculated as the difference between the average response to the preferred texture and the average response to the nonpreferred texture. (**c**) The mean texture response amplitudes of all texture discriminative neurons, in trials where mice did not lick during the texture window (no early licks). (**d**) Selectivity index of neurons in (**c**). (**a**,**b**: S1: 1213 neurons; PPC-A: 239neurons; PPC-RL: 481 neurons; **c**,**d**: S11486 neurons; PPC-A 400 neurons; PPC-RL 618 neurons; Wilcoxon rank-sum test; ***$P < 0.001$; Supplementary Table 1).

https://doi.org/10.1038/s41593-023-01534-x

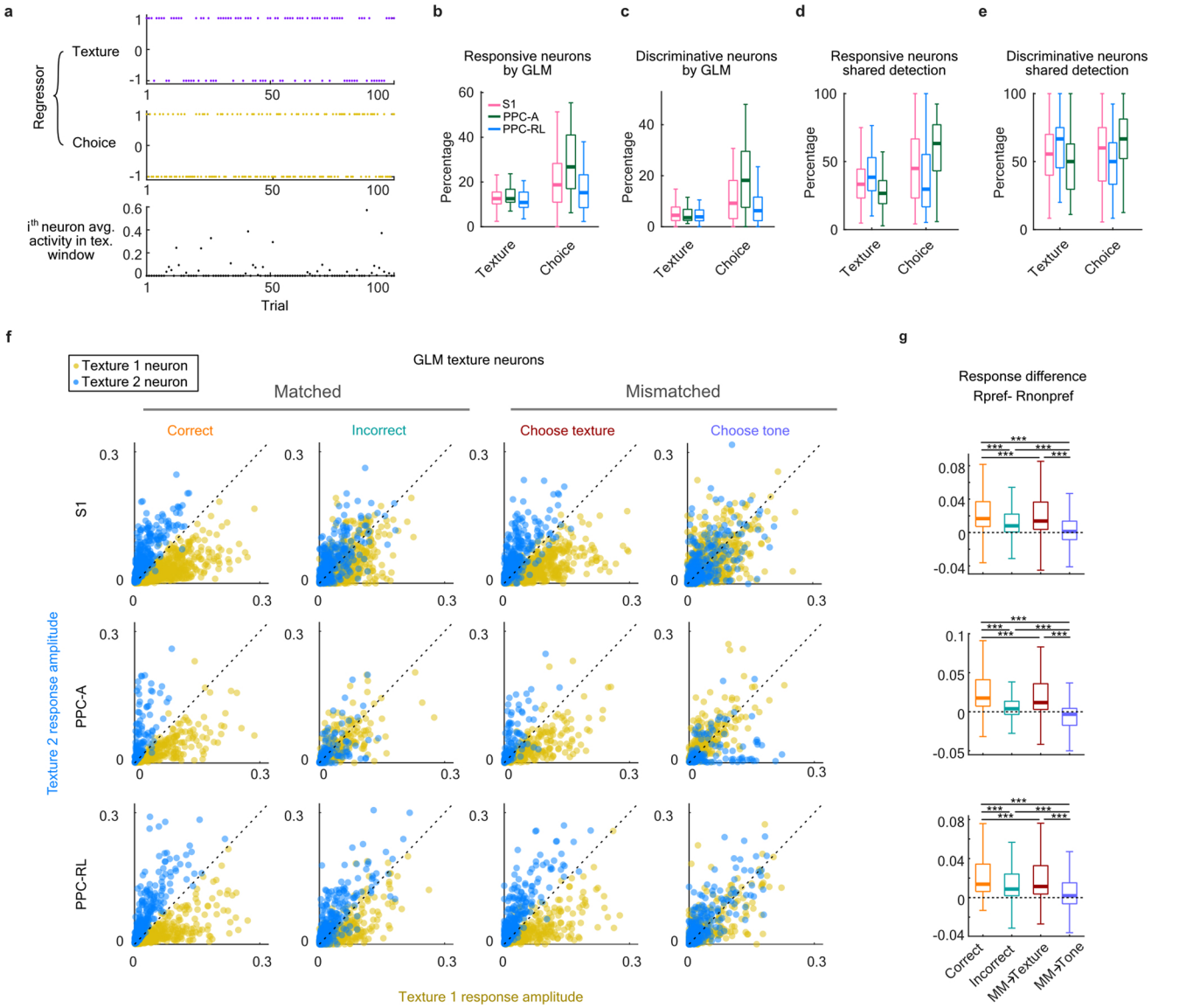

Extended Data Fig. 5 | Response amplitude of texture-discriminative neurons identified by GLM model. (**a**) Scheme of GLM regression. Two discrete regressors, texture and choice, were used to model the average activity during choice window, for each neuron. Regression performance was measured by the correlation value of predicted activity with real activity. Task responsive neurons were identified by comparing these correlation values against models generated by shuffling one regressor at a time. (**b**) Percentage of texture- and choice-responsive neurons identified by GLM from texture window. (**c**) Percentage of texture- and choice-discriminative neurons identified by GLM from texture window. (**d**) Percentage of task responsive neurons in Fig. 2d that are also identified by GLM method. (**e**) Percentage of task discriminative neurons in Fig. 2e that are also identified by GLM method. (**f**) The mean texture response amplitudes of all GLM-identified texture discriminative neurons during texture window. Each dot represents the response of one neuron in one imaging session. (**g**) Selectivity index of texture discriminative neurons in (**f**). (S1: 1478 neurons; PPC-A: 458 neurons; PPC-RL: 910 neurons; Wilcoxon rank-sum test; ***$P < 0.001$; Supplementary Table 1).

https://doi.org/10.1038/s41593-023-01534-x

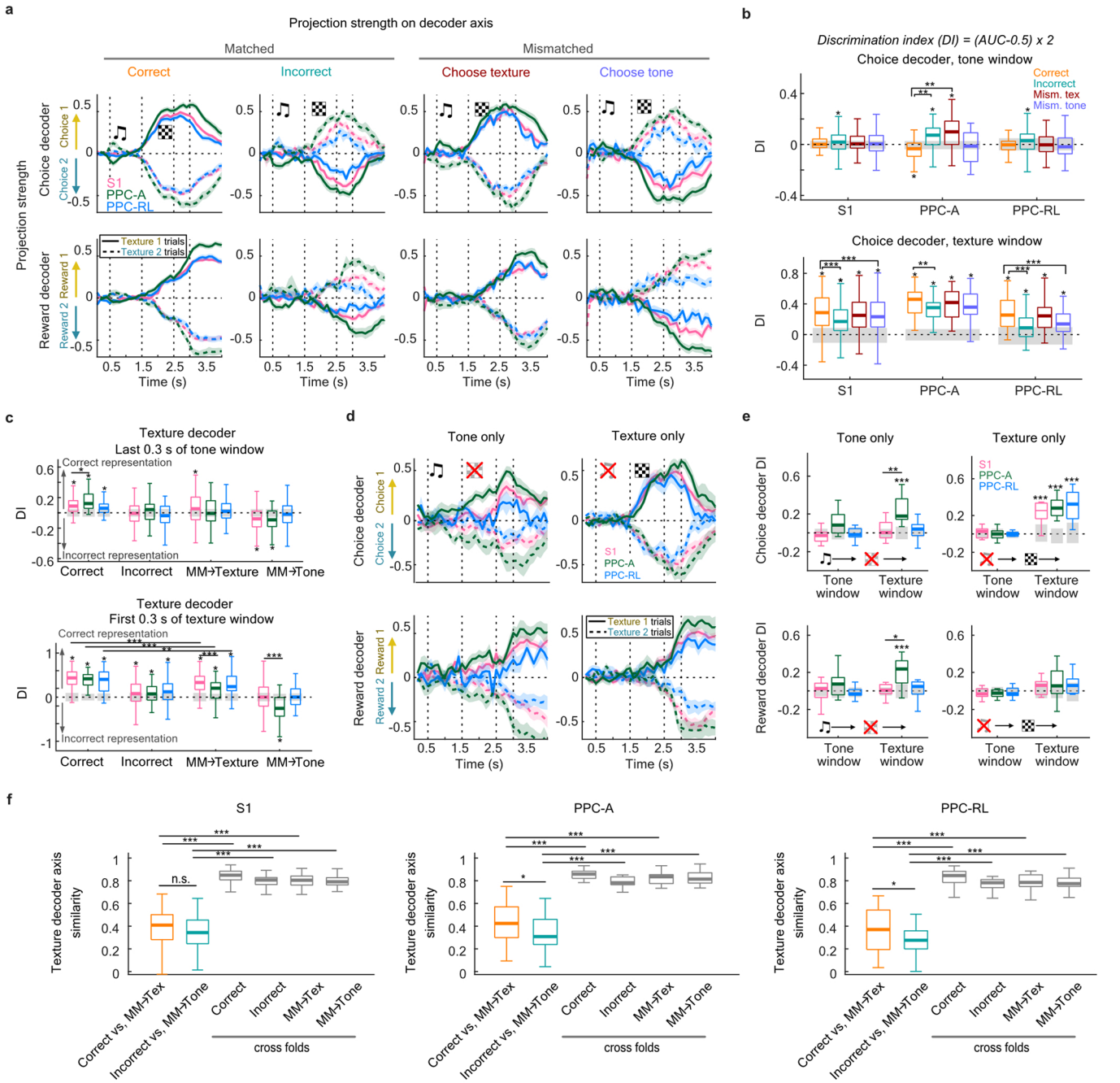

Extended Data Fig. 6 | Choice and reward encoding in S1 and PPC. (**a**) Neuronal population encoding of choice (top panels) and reward (bottom panels). Line colors indicate area identity; solid and dash lines indicate texture identity of the trial. (**b**) Discrimination index (DI) of the choice decoder and reward decoder, in the tone window and texture window, separately. Asterisks above each box indicate the significance with shuffled data (gray bars) where neuron identities were shuffled, while trial and time correspondence were kept the same. Asterisks across boxes indicate comparison between trial types. (**c**) DI of texture decoder before texture onset (last 0.3 s of tone window, top panel) and after texture onset (first 0.3 s of texture window, bottom panel). (**d**) Neuronal population encoding strength of choice (top panels) and reward (bottom panels) in single modality experiments. (**e**) DI of choice decoder and reward decoder in single modality experiments, in tone window and texture window, separately. Asterisks are represented as in (**b**). (**f**) Texture decoder axis similarity (projection axis correlation) from decoders trained with each trial type, separately. For each trial type, trials were randomly split into two subsets, and two separate decoders were trained. The averaged axis was used for decoder similarity between trial types, and cross folds represent the similarity between two independent decoders trained with the same trial type. Sessions with less than 30 trials for each trial type were excluded to ensure enough training samples. (S1: 14 mice, 118 sessions; PPC-RL: 14 mice, 78 sessions; PPC-A: 9 mice, 40 sessions; $^{*}P < 0.05$; $^{**}P < 0.01$; $^{***}P < 0.001$; Supplementary Table 1).

https://doi.org/10.1038/s41593-023-01534-x

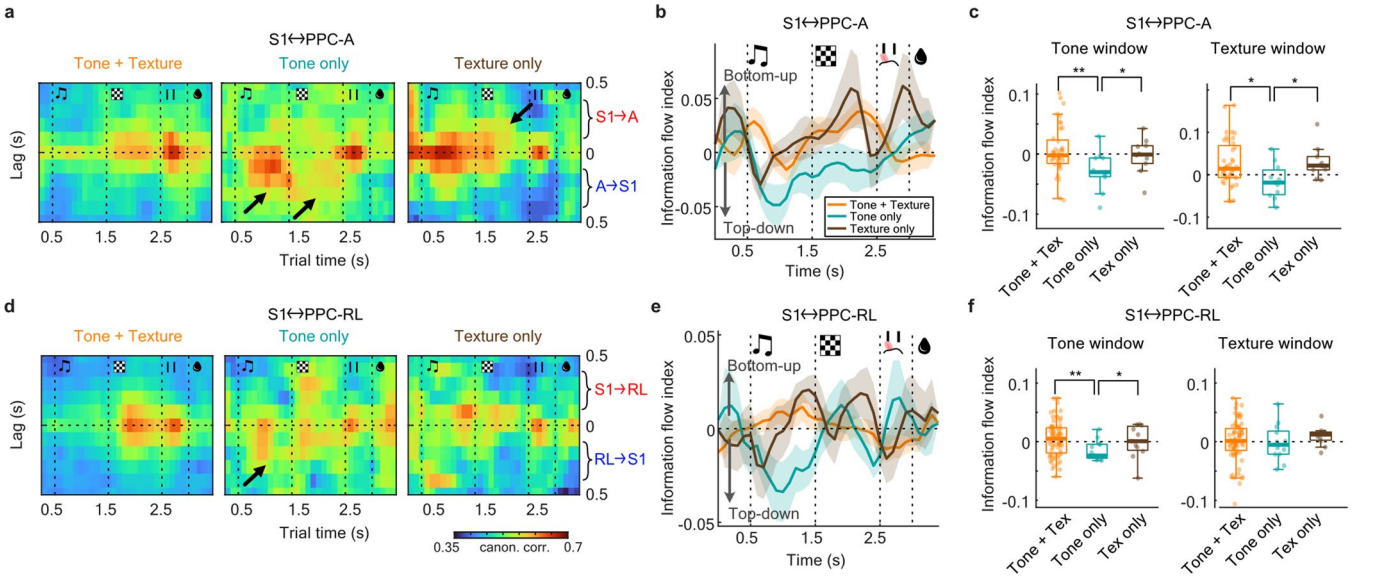

Extended Data Fig. 7 | Interaction between S1 and PPC in single modality trials. (**a**) Lagged canonical correlation between S1 and PPC-A averaged across all sessions, for matched stimuli (tone + texture), tone only, and texture only conditions. Note the stronger top-down (A to S1) interaction in tone-only condition and stronger bottom-up (S1 to A) interaction in texture only condition. (**b**) Information flow index computed from (**a**). (**c**) Quantification of information flow index between S1 and PPC-A. (**d**) Averaged lagged canonical correlation between S1 and PPC-RL. Note the slightly stronger top-down (RL to S1) interaction during tone window in tone only condition. (**e**) Information flow index computed from (**d**). (**f**) Quantification of information flow index between S1 and PPC-RL (S1↔PPC-A: 9 mice, 40 sessions; S1↔PPC-RL: 13 mice, 71 sessions; Wilcoxon rank-sum test; $^{*}P < 0.05$; $^{**}P < 0.01$; Supplementary Table 1).

https://doi.org/10.1038/s41593-023-01534-x

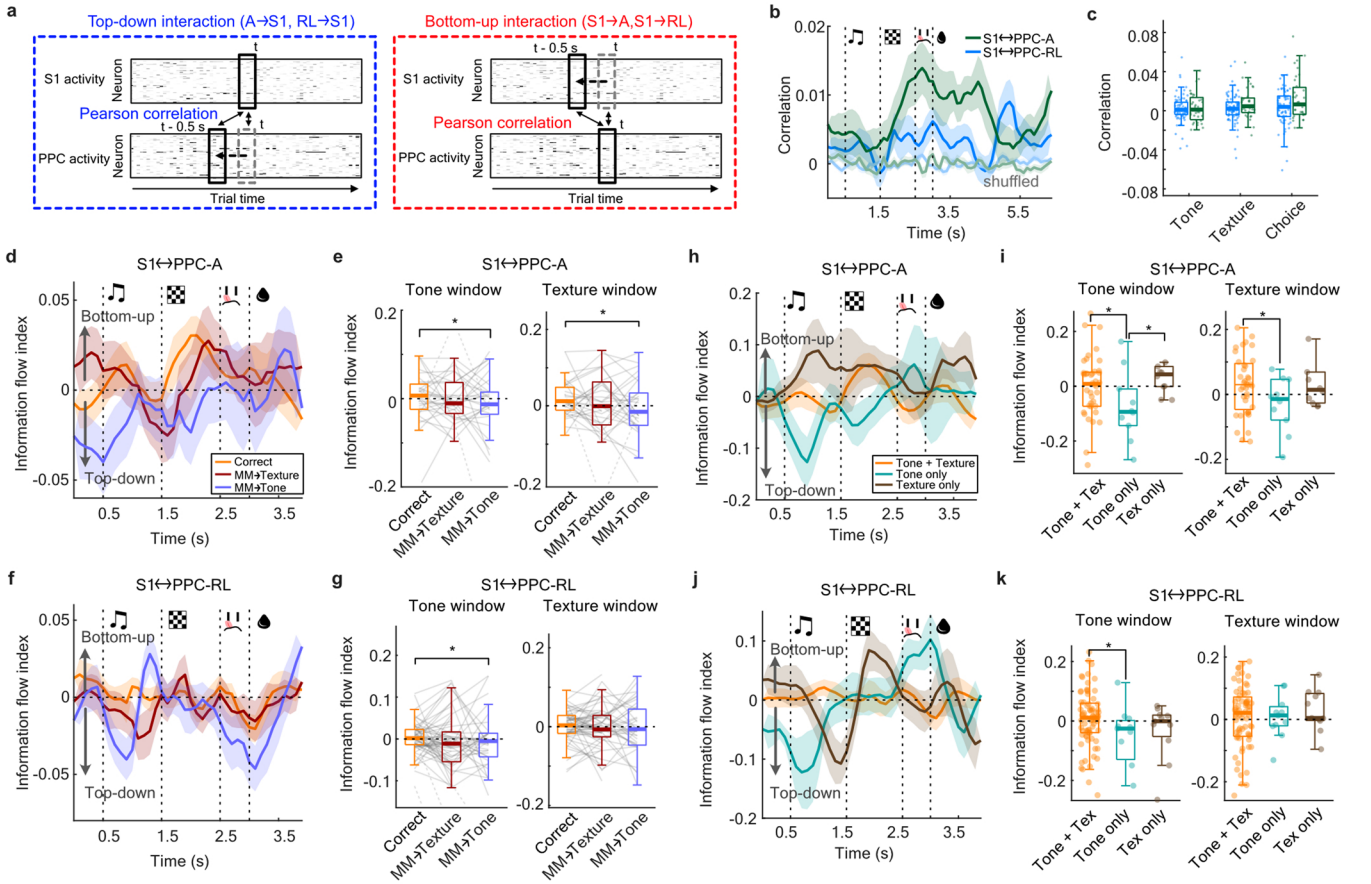

Extended Data Fig. 8 | Top-down and bottom-up interaction analysis with Pearson correlation. (**a**) Top-down and bottom-up interaction strength were evaluated in the same way as Fig. 6a, except that the correlation was calculated using Pearson correlation instead of CCA. (**b**) Population correlation between S1 and PPC-A (green), and S1 and PPC-RL (blue). (**c**) Average canonical correlation strength of (**b**) in each task window. (**d**) Information flow index (IFI) of S1–PPC-A interaction using Pearson correlation. (**e**) Quantification of (**d**). (**f**) Information flow index of S1–PPC-RL interaction using Pearson correlation. (**g**) Quantification of (**f**). (**h**) Information flow index of S1–PPC-A interaction in single modality conditions. (**i**) Quantification of (h). (**j**) Information flow index of S1–PPC-RL interaction in single modality conditions. (**k**) Quantification of (**j**). (S1↔PPC-A: 9 mice, 40 sessions; S1↔PPC-RL: 13 mice, 71 sessions; Wilcoxon signed-rank test; $^*P < 0.05$; Supplementary Table 1).

https://doi.org/10.1038/s41593-023-01534-x

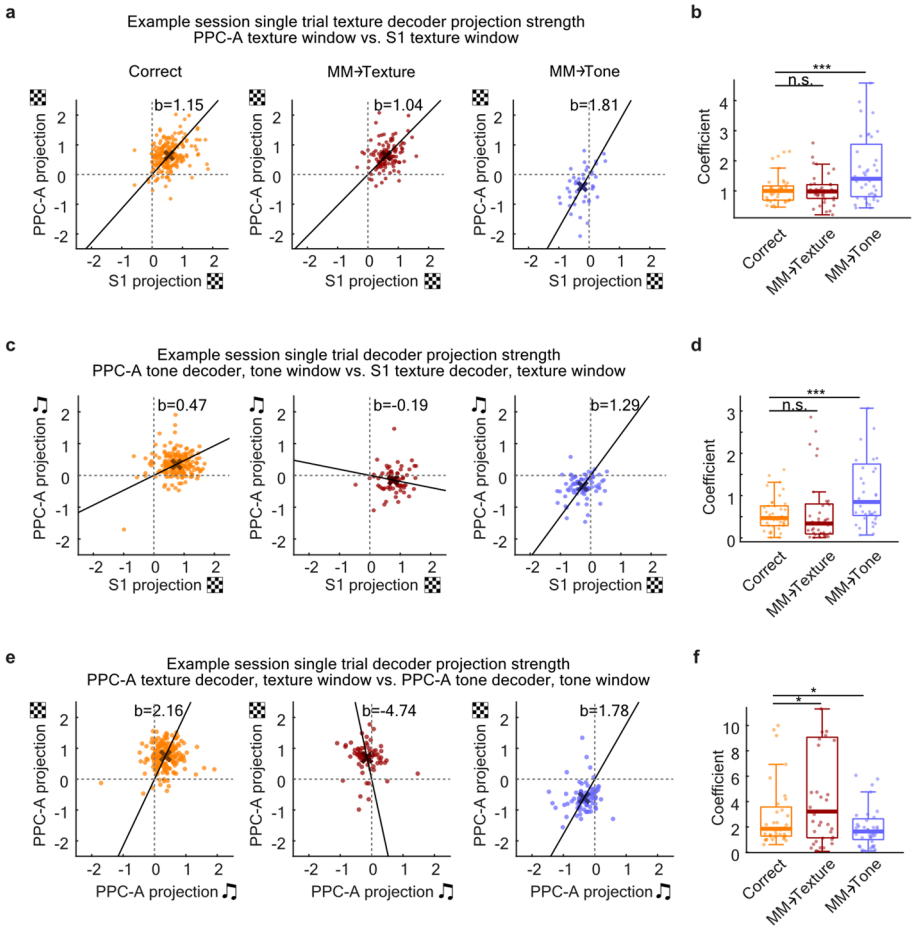

Extended Data Fig. 9 | Trial-to-trial population encoding strength analysis of S1 and PPC-A. (**a**) Trial-to-trial PPC-A texture encoding strength (averaged texture decoder projection strength in texture window) vs. S1 texture encoding strength, in an example session. The projection strength is averaged within the corresponding task window and z-scored within each session. Response coefficient is calculated using the center of mass of all data points (y value divided by x value). (**b**) PPC-A vs. S1 texture response coefficient of all sessions, using absolute values. (**c**) Trial-to-trial PPC-A tone encoding strength (averaged tone decoder projection strength in tone window) vs. S1 texture encoding strength (texture decoder projection strength in texture window), in an example session. (**d**) PPC-A tone vs. S1 texture response coefficient of all sessions. (**e**) Trial-to-trial PPC-A texture encoding strength vs. tone encoding strength, in an example session. (**f**) PPC-A texture vs. tone response coefficient of all sessions. (S1: 14 mice, 118 sessions; PPC-RL: 14 mice, 78 sessions; PPC-A: 9 mice, 40 sessions; Wilcoxon signed-rank test; $^{*}P < 0.05$; $^{***}P < 0.001$; n.s. nonsignificant; Supplementary Table 1).

https://doi.org/10.1038/s41593-023-01534-x

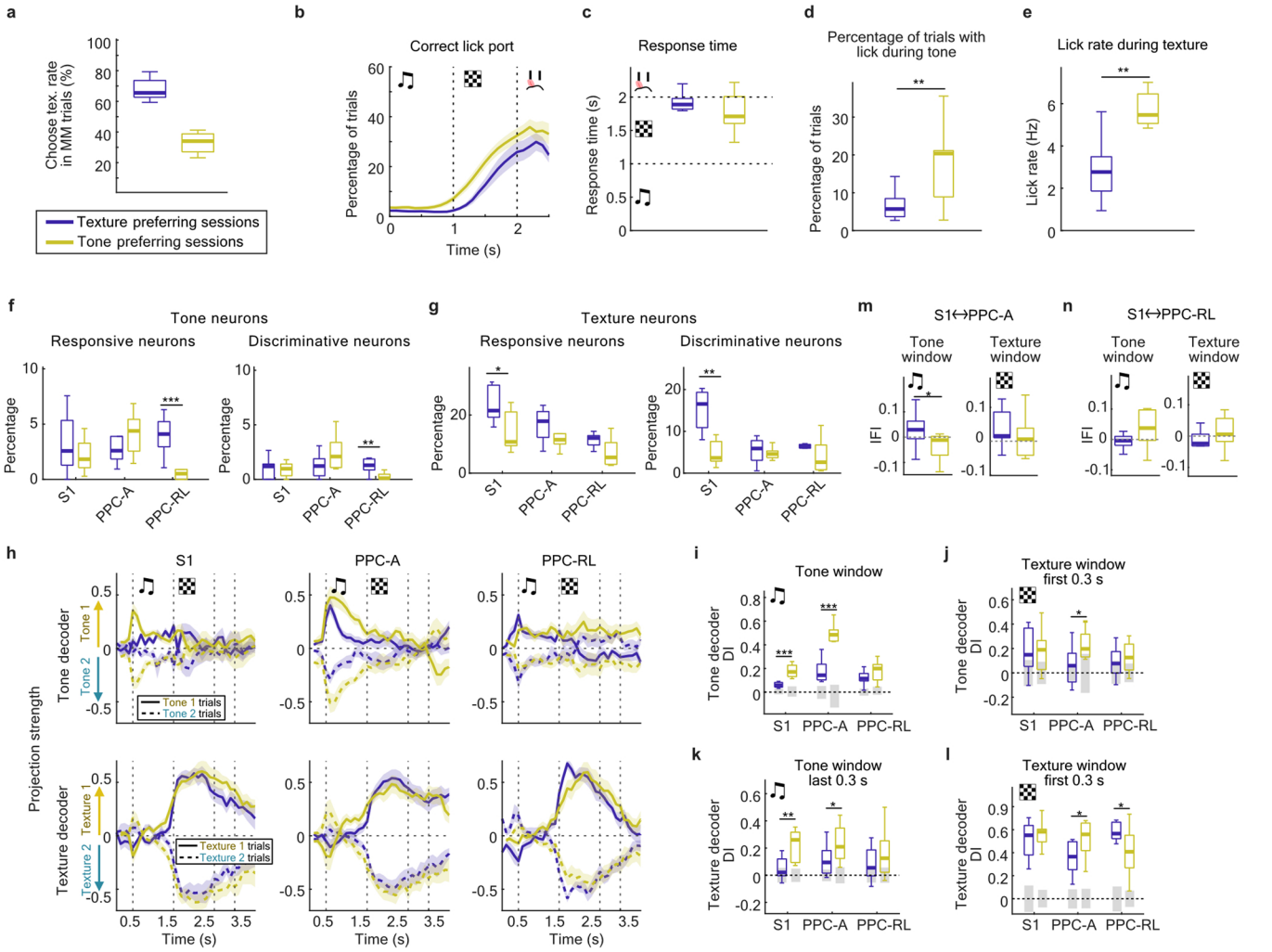

Extended Data Fig. 10 | Texture-preferring sessions and tone-preferring sessions. (**a**) Rate of choosing texture in mismatch trials, in 10 highest sessions (purple) and 10 lowest sessions (yellow). The 10 highest sessions where mice were prone to choosing texture in mismatch trials were defined as texture-preferring sessions. The 10 lowest sessions were defined as tone-preferring sessions. Color code remains the same for the rest of this figure. (**b**) Lick rate on the correct lick port. (**c**) Response time. (**d**) Percentage of trial with lick during tone. (**e**) Lick rate during texture. (**f**) Percentage of tone responsive neurons (left) and tone discriminative neurons (right) in these sessions. (**g**) Percentage of texture responsive neurons (left) and texture discriminative neurons (right) in these sessions. (**h**) Neuronal population encoding strength of tone (top panels) and texture (bottom panels) in correct trials. Solid and dash lines indicate texture identity of the trial. (**i**) Tone decoder discrimination index (DI) in tone window. (**j**) Tone decoder DI in the first 0.3 s of texture window. (**k**) Texture decoder AUC in the last 0.3 s of tone window. (**l**) Texture decoder DI in the first 0.3 s of texture window. (**m**) Information flow index of S1–PPC-A interaction in tone window (left) and texture window (right), during correct trials. (**n**) Information flow index of S1–PPC-RL interaction in the last 0.3 s of tone window (left) and the first 0.3 s of texture window (right), during correct trials. (10 sessions for each condition; 3 mice for texture-preferring sessions, 4 mice for tone-preferring sessions; Wilcoxon rank-sum test; $^{*}P < 0.05$; $^{**}P < 0.01$; $^{***}P < 0.001$; Supplementary Table 1).

nature portfolio

Corresponding author(s): Shuting Han, Fritjof Helmchen

Last updated by author(s): Nov 6, 2023

Reporting Summary

Nature Portfolio wishes to improve the reproducibility of the work that we publish. This form provides structure for consistency and transparency in reporting. For further information on Nature Portfolio policies, see our Editorial Policies and the Editorial Policy Checklist.

Statistics

For all statistical analyses, confirm that the following items are present in the figure legend, table legend, main text, or Methods section.

n/a	Confirmed	
☐	☒	The exact sample size (*n*) for each experimental group/condition, given as a discrete number and unit of measurement
☐	☒	A statement on whether measurements were taken from distinct samples or whether the same sample was measured repeatedly
☐	☒	The statistical test(s) used AND whether they are one- or two-sided *Only common tests should be described solely by name; describe more complex techniques in the Methods section.*
☒	☐	A description of all covariates tested
☐	☒	A description of any assumptions or corrections, such as tests of normality and adjustment for multiple comparisons
☒	☐	A full description of the statistical parameters including central tendency (e.g. means) or other basic estimates (e.g. regression coefficient) AND variation (e.g. standard deviation) or associated estimates of uncertainty (e.g. confidence intervals)
☐	☒	For null hypothesis testing, the test statistic (e.g. *F*, *t*, *r*) with confidence intervals, effect sizes, degrees of freedom and *P* value noted *Give P values as exact values whenever suitable.*
☒	☐	For Bayesian analysis, information on the choice of priors and Markov chain Monte Carlo settings
☒	☐	For hierarchical and complex designs, identification of the appropriate level for tests and full reporting of outcomes
☒	☐	Estimates of effect sizes (e.g. Cohen's *d*, Pearson's *r*), indicating how they were calculated

Our web collection on statistics for biologists contains articles on many of the points above.

Software and code

Policy information about availability of computer code

Data collection	Behavior training: custom LabVIEW software (HIFOTDT 1.2.7) Body camera: custom LabVIEW software (2014) Widefield imaging: custom LabVIEW software (2014) Multiarea two photon imaging: custom C++ software (Scope, http://rkscope.sourceforge.net)
Data analysis	Two photon data processing: open source python pipeline Suite2p (https://github.com/MouseLand/suite2p) Canonical correlation analysis: open source MATLAB package (https://github.com/joao-semedo/canonical-correlation-maps) All other analysis was performed with custom written MATLAB code using MATLAB R2018b.

For manuscripts utilizing custom algorithms or software that are central to the research but not yet described in published literature, software must be made available to editors and reviewers. We strongly encourage code deposition in a community repository (e.g. GitHub). See the Nature Portfolio guidelines for submitting code & software for further information.

Data

Policy information about availability of data

All manuscripts must include a data availability statement. This statement should provide the following information, where applicable:

- Accession codes, unique identifiers, or web links for publicly available datasets
- A description of any restrictions on data availability
- For clinical datasets or third party data, please ensure that the statement adheres to our policy

A subset of the data is available at a Zenodo repository due to space limitation (https://zenodo.org/records/10078711). The full dataset is available from the corresponding authors upon request.

Human research participants

Policy information about studies involving human research participants and Sex and Gender in Research.

Reporting on sex and gender	No human subjects participated in this study.
Population characteristics	No human subjects participated in this study.
Recruitment	No human subjects participated in this study.
Ethics oversight	No human subjects participated in this study.

Note that full information on the approval of the study protocol must also be provided in the manuscript.

Field-specific reporting

Please select the one below that is the best fit for your research. If you are not sure, read the appropriate sections before making your selection.

☒ Life sciences ☐ Behavioural & social sciences ☐ Ecological, evolutionary & environmental sciences

For a reference copy of the document with all sections, see nature.com/documents/nr-reporting-summary-flat.pdf

Life sciences study design

All studies must disclose on these points even when the disclosure is negative.

Sample size	No statistical methods were used to pre-determine sample sizes, but our sample sizes are similar to those reported in previous publications (see references 10, 26, 59). In behavioral experiments where neuronal populations were recorded, previous literature typically report 5-15 mice per experiment group, and 3-5 sessions per mouse. Our sample size was in accordance with these practice.
Data exclusions	All data exclusion criteria are described in the Methods section. Among all the mice, two were excluded from imaging studies due to decayed cranial window quality; one additional mouse was excluded from CCA analysis due to decayed S1 quality.
Replication	All analysis were performed across multiple mice, and multiple sessions for each mouse and each imaging condition (typically 3-7 session per condition per mouse). The results were reproduced, as indicated by the statistical tests. Cross-validation was applied where it is applicable (Fig. 4-6), and the analysis results were reproduced with multiple models generated on separate subsets of data within session.
Randomization	Group assignment was inclusive. Out of all mice, 9 mice were included in both experiment groups (S1-PPCA and S1-PPCRL imaging sessions, as well as single modality experiments), and 5 additional mice were included only in S1-PPCRL imaging sessions.
Blinding	No blinding was done in this study. Data of different experiment designs was collected on the same mice, therefore blinding during data collection was not applicable. The analysis pipeline was developed according to the biological questions we wanted to address, and applied to each group separately afterwards.

Reporting for specific materials, systems and methods

We require information from authors about some types of materials, experimental systems and methods used in many studies. Here, indicate whether each material, system or method listed is relevant to your study. If you are not sure if a list item applies to your research, read the appropriate section before selecting a response.

Materials & experimental systems

n/a	Involved in the study
☒	☐ Antibodies
☒	☐ Eukaryotic cell lines
☒	☐ Palaeontology and archaeology
☐	☒ Animals and other organisms
☒	☐ Clinical data
☒	☐ Dual use research of concern

Methods

n/a	Involved in the study
☒	☐ ChIP-seq
☒	☐ Flow cytometry
☒	☐ MRI-based neuroimaging

Animals and other research organisms

Policy information about studies involving animals; ARRIVE guidelines recommended for reporting animal research, and Sex and Gender in Research

Laboratory animals	The detailed animal information is reported in the Methods section. Strains used in this study: (1) RasGRF2a-dCre;CamK2a-tTA;TITL-GCaMP6f; (2) GP5.17; (3) Snap25-IRES2-Cre-D;CamK2a-tTA;TITL-GCaMP6f; (4) RasGRF2a-dCre;tTA2-GCaMP6f. Both sexes were used. Mice were 2.5-4 months old at the beginning of behavior training, and 3-5 months old at the time of experiment. Mice were housed on a 12-h reversed light/dark cycle at an ambient temperature of between 21 °C and 23 °C and humidity between 55% and 60%.
Wild animals	No wild animals were used.
Reporting on sex	Both sexes were used (9 males, 8 females) and randomly assigned to each group. The analysis was done using data from both sexes together. No sex-based analysis was performed, since sex was not a variable of interest in this study.
Field-collected samples	This study did not involve samples collected from the field.
Ethics oversight	All experimental procedures were carried out in accordance with the guidelines of the Federal Veterinary Office of Switzerland and were approved by the Cantonal Veterinary Office in Zurich.

Note that full information on the approval of the study protocol must also be provided in the manuscript.